Text Supplement for ScholarWorks@UA collection
Hypocenter estimation for 14 earthquakes in south-central Alaska (1929–1975)

Anthony Lomax, Vipul Silwal, Carl Tape

May 2, 2018

Attribution: If you use these files, please cite *Silwal et al.* (2018) and *Lomax et al.* (2018).

Overview

These figures are a supplement to *Silwal et al.* (2018), which examined all 11 earthquakes $M_w \geq 5.8$, 1904–1976, in the ISC-GEM catalog (*Storchak et al.*, 2013; *International Seismological Centre*, 2018) in the Cook Inlet and Susitna region. Here we provide two sets of figures for the earthquakes. The first set of figures (Figure A1–A14) shows the global coverage of P and S arrival times used in the hypocenter estimation. The second set of figures (Figure B1–B14) is based on the cloud of posterior hypocenters obtained using NonLinLoc (*Lomax et al.*, 2000, 2014). For each posterior epicenter we calculate the depth of the subduction interface (*Li et al.*, 2013), and then examine the likelihood that an earthquake occurred in the overriding crust, on the subduction interface, or within the slab, as described in *Silwal et al.* (2018). In addition to plotting the posterior epicenters in map view (e.g., Figure B1a), we also plot felt reports from *Brockman et al.* (1988) that are within the plotted region.

The search region here is slightly larger (longitude -152 to -149, latitude 60 to 63) than that used in *Silwal et al.* (2018) (longitude -151.75 to -149.5, latitude 60.5 to 62.5), and as a result, there are three additional events here: 1929-07-03, 1937-10-24, and 1949-09-27. The date range in the title, 1929–1975, indicates that there were no events in the ISC-GEM catalog in the target region from 1904-01-01 to 1929-01-01 and in the year of 1976.

A summary of files in the collection is listed in the following table:

file name	description
scholarworks_lomax.pdf	this file: summary of collection, figure of station coverage for each earthquake (Figures A1–A14), summary figure for each earthquake (Figures B1–B14)
nll_14events_cook_susitna_alaska.zip	zipped set of output files from NonLinLoc for 14 earthquakes in the Cook Inlet and Susitna region of southern Alaska

List of IDs for the 14 events. The columns are: (1) the ISC-GEM origin time yyyy-mm-dd HH:MM:SS.FFF, (2) ISC-GEM catalog ID, (3) output file ID from NonLinLoc.

19290703005304360	908180	607282694
19330427023607770	905539	905539
19330612152341910	905632	607283695
19330613221951710	905637	607283698
19330619184746480	905648	607283702
19340618091352170	904995	904995
19361023062421340	903895	606304509
19371024113602720	903311	606304726
19410730015129880	900931	900931
19431103143220840	900071	900071
19490927153046360	896889	896889
19541003111848530	891130	891130
19741229182501390	734885	734885
19750101035513370	732776	732776

Numbers of P and S picks used to relocate each earthquake (see Figures A1–A14 below):

19290703 :	35 P picks	28 S picks	39 unique stations with P or S
19330427 :	174 P picks	158 S picks	179 unique stations with P or S
19330612 :	22 P picks	20 S picks	31 unique stations with P or S
19330613 :	69 P picks	62 S picks	78 unique stations with P or S
19330619 :	36 P picks	39 S picks	48 unique stations with P or S
19340618 :	98 P picks	89 S picks	104 unique stations with P or S
19361023 :	154 P picks	132 S picks	161 unique stations with P or S
19371024 :	66 P picks	54 S picks	75 unique stations with P or S
19410730 :	102 P picks	95 S picks	107 unique stations with P or S
19431103 :	137 P picks	136 S picks	137 unique stations with P or S
19490927 :	164 P picks	162 S picks	170 unique stations with P or S
19541003 :	346 P picks	223 S picks	263 unique stations with P or S
19741229 :	286 P picks	16 S picks	245 unique stations with P or S
19750101 :	426 P picks	66 S picks	346 unique stations with P or S

References

Brockman, S. R., A. F. Espinosa, and J. A. Michael (1988), *Catalog of Intensities and Magnitudes for Earthquakes in Alaska and the Aleutian Islands—1786–1981*, U.S. Geol. Survey Bulletin 1840.

Doser, D. I., and W. A. Brown (2001), A study of historic earthquakes of the Prince William Sound, Alaska, Region, *Bull. Seismol. Soc. Am.*, *91*(4), 842–857.

International Seismological Centre (2018), ISC-GEM Global Instrumental Earthquake Catalogue, Version 5.0, released on 2018-02-27.

Li, J., G. A. Abers, Y. Kim, and D. Christensen (2013), Alaska megathrust 1: Seismicity 43 years after the great 1964 Alaska megathrust earthquake, *J. Geophys. Res.*, *118*, 4861–4871, doi:10.1002/jgrb.50358.

Lomax, A., J. Virieux, P. Volant, and C. Berge (2000), Probabilistic earthquake location in 3D and layered models: Introduction of a Metropolis-Gibbs method and comparison with linear locations, in *Advances in Seismic Event Location*, edited by C. H. Thurber and N. Rabinowitz, pp. 101–134, Kluwer, Amsterdam.

Lomax, A., A. Michelini, and A. Curtis (2014), Earthquake location, direct, global-search methods, in *Encyclopedia of Complexity and System Science*, edited by R. A. Meyers, 2 ed., pp. 1–33, Springer, New York, doi:10.1007/978-3-642-27737-5_150-2.

Lomax, A., V. Silwal, and C. Tape (2018), Hypocenter estimation for 14 earthquakes in south-central Alaska (1929–1975), ScholarWorks@UA: descriptor file and zipped set of text files for each earthquake.

Silwal, V., C. Tape, and A. Lomax (2018), Crustal earthquakes in the Cook Inlet and Susitna region of southern Alaska, *Tectonophysics* (in prep).

Storchak, D. A., D. Di Giacomo, I. Bondár, E. R. Engdahl, J. Harris, W. H. K. Lee, A. Villasenor, and P. Bormann (2013), Public release of the ISC–GEM Global Instrumental Earthquake Catalogue (1900–2009), *Seismol. Res. Lett.*, *84*(5), 810–815, doi:10.1785/0220130034.

(a)

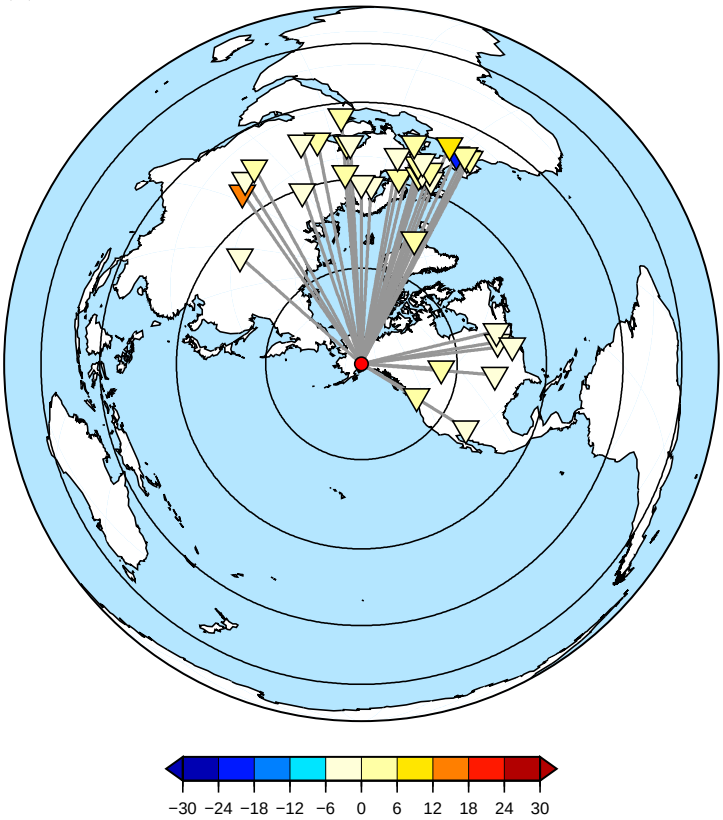

(b)

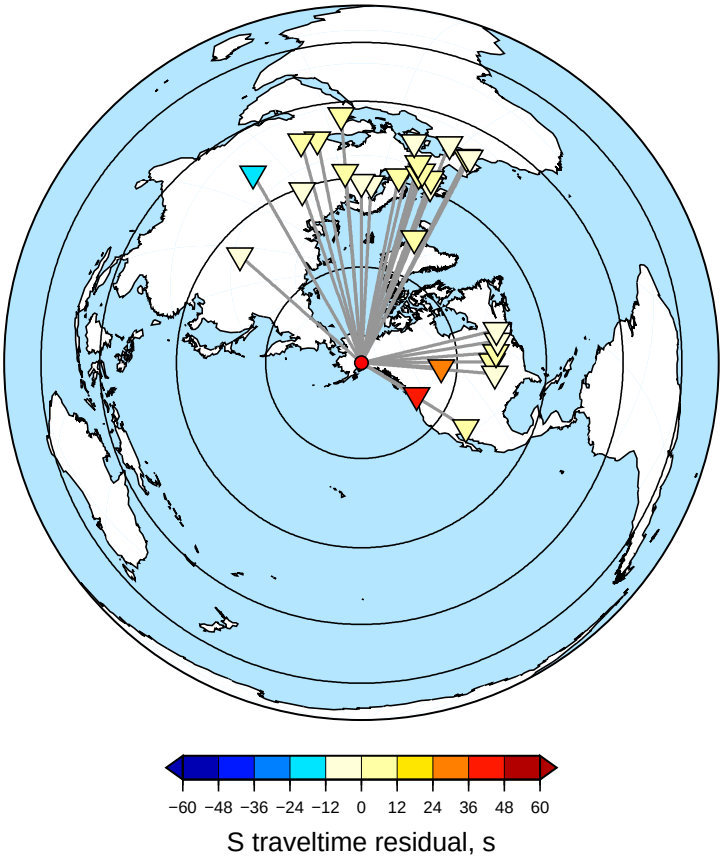

Figure A1: Station coverage of P and S arrival times for event 19290703. The color of each triangle corresponds to the traveltime difference between the observed time and the time predicted using the maximum likelihood hypocenter and origin time, with a 1D Earth model. See also Figure B1.

(a)

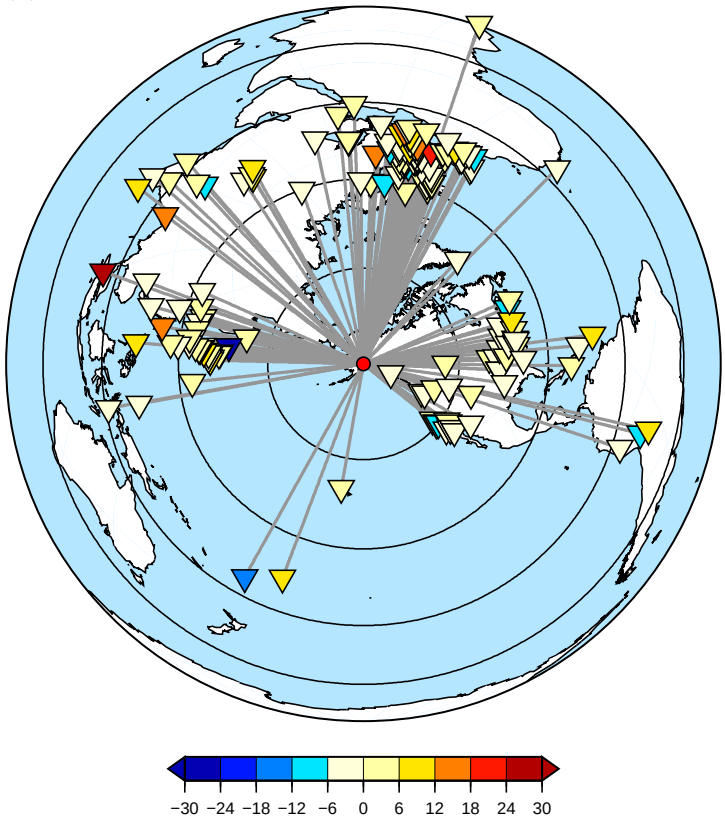

(b)

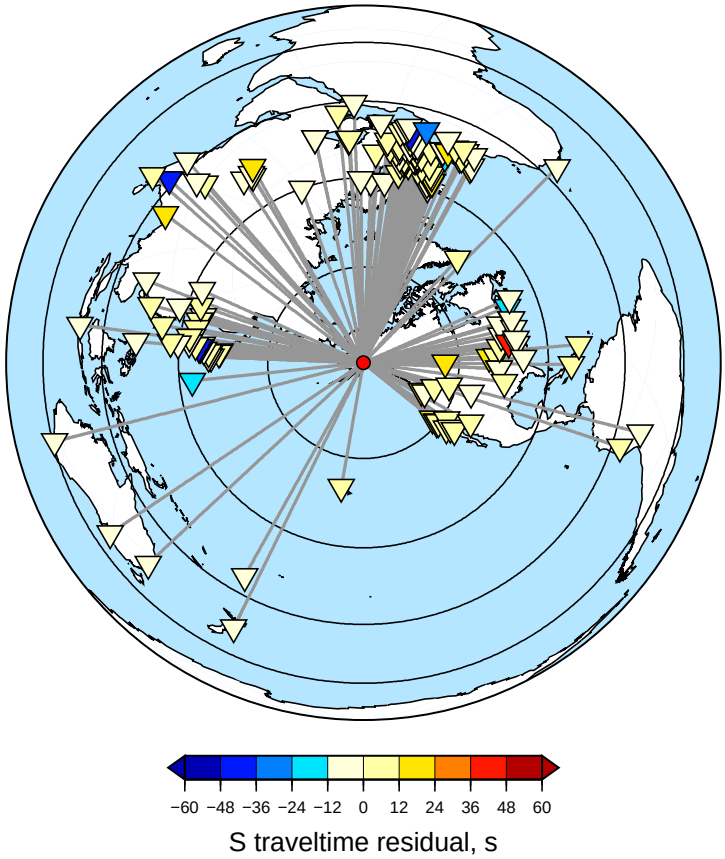

Figure A2: Station coverage of P and S arrival times for event 19330427. The color of each triangle corresponds to the traveltime difference between the observed time and the time predicted using the maximum likelihood hypocenter and origin time, with a 1D Earth model. See also Figure B2.

(a)

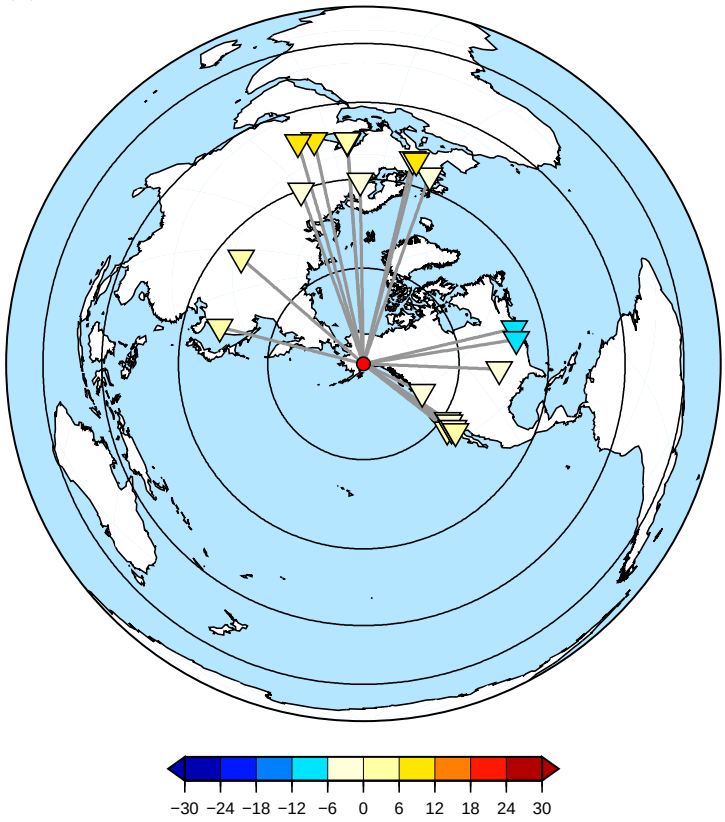

(b)

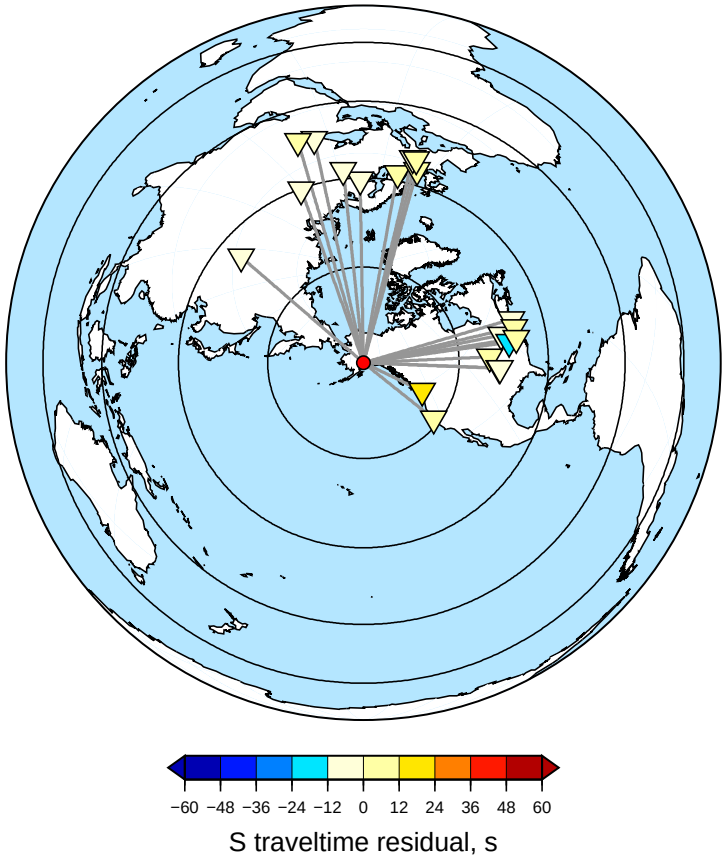

Figure A3: Station coverage of P and S arrival times for event 19330612. The color of each triangle corresponds to the traveltime difference between the observed time and the time predicted using the maximum likelihood hypocenter and origin time, with a 1D Earth model. See also Figure B3.

(a)

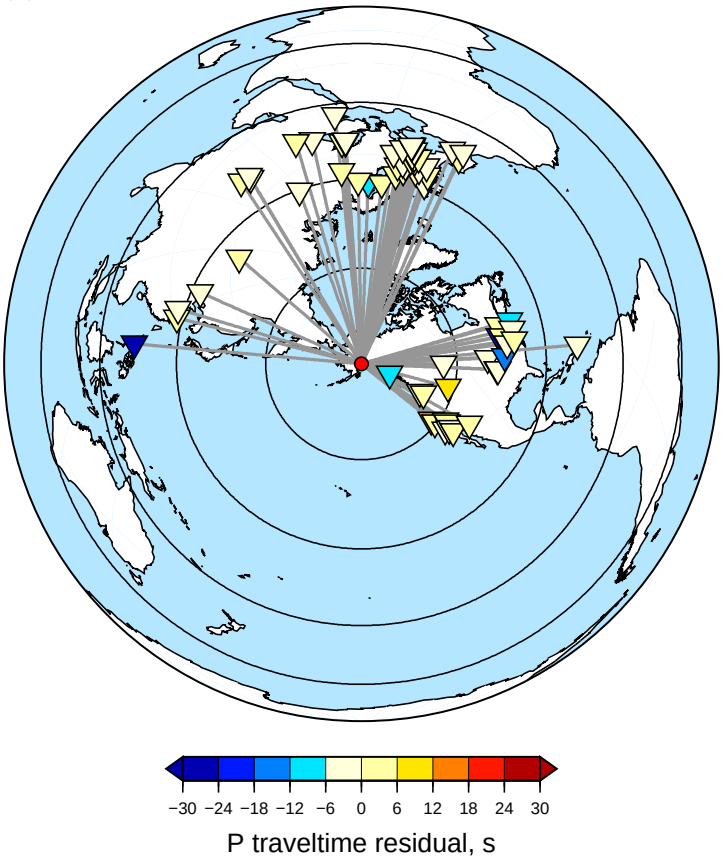

(b)

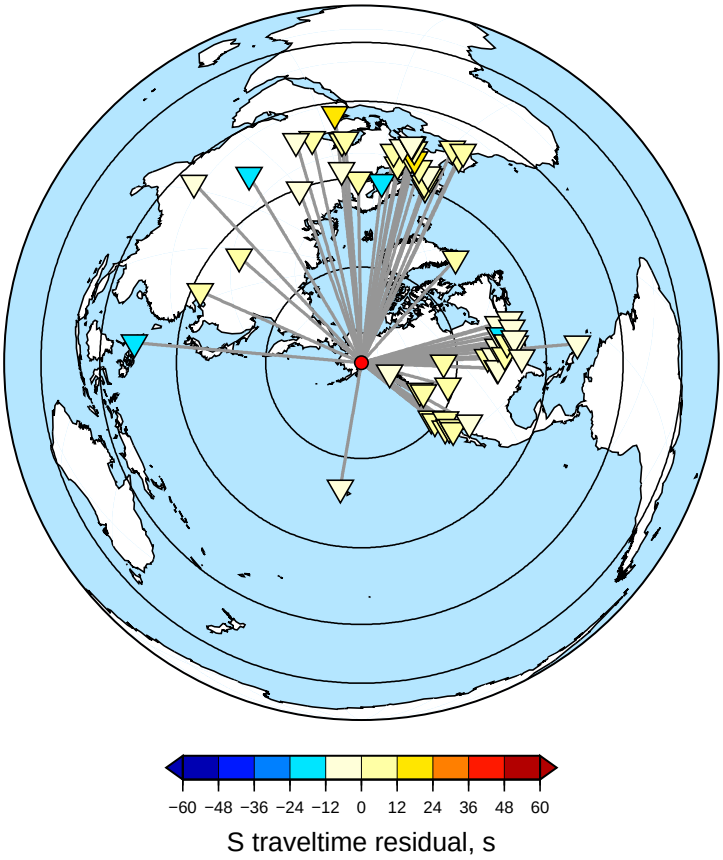

Figure A4: Station coverage of P and S arrival times for event 19330613. The color of each triangle corresponds to the traveltime difference between the observed time and the time predicted using the maximum likelihood hypocenter and origin time, with a 1D Earth model. See also Figure B4.

(a)

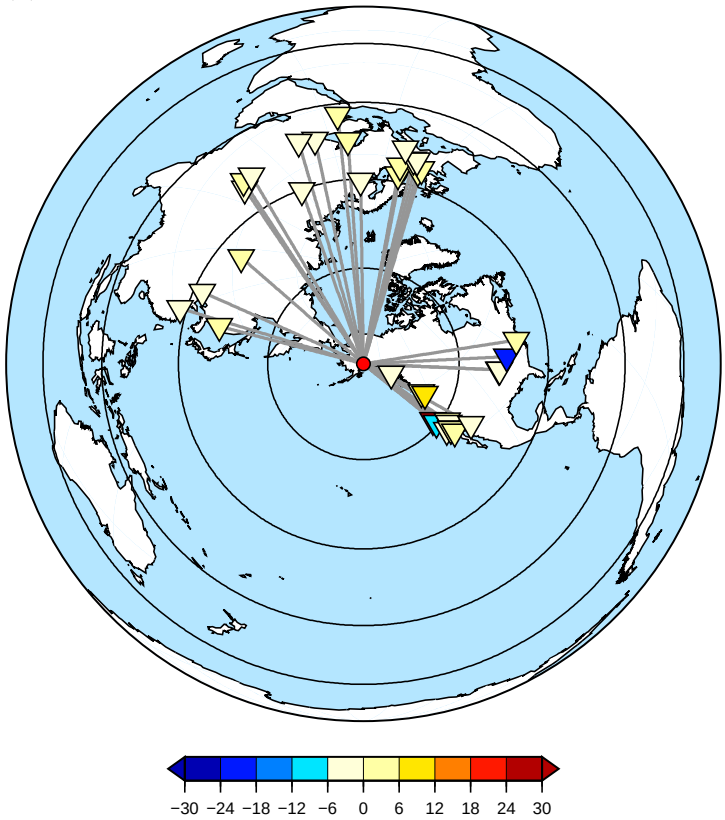

(b)

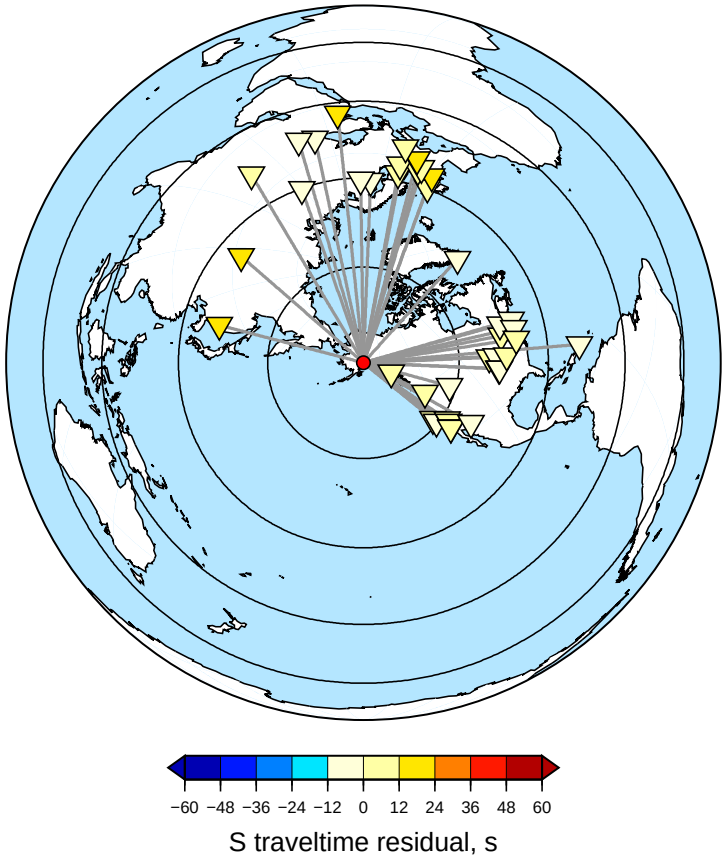

Figure A5: Station coverage of P and S arrival times for event 19330619. The color of each triangle corresponds to the traveltime difference between the observed time and the time predicted using the maximum likelihood hypocenter and origin time, with a 1D Earth model. See also Figure B5.

(a)

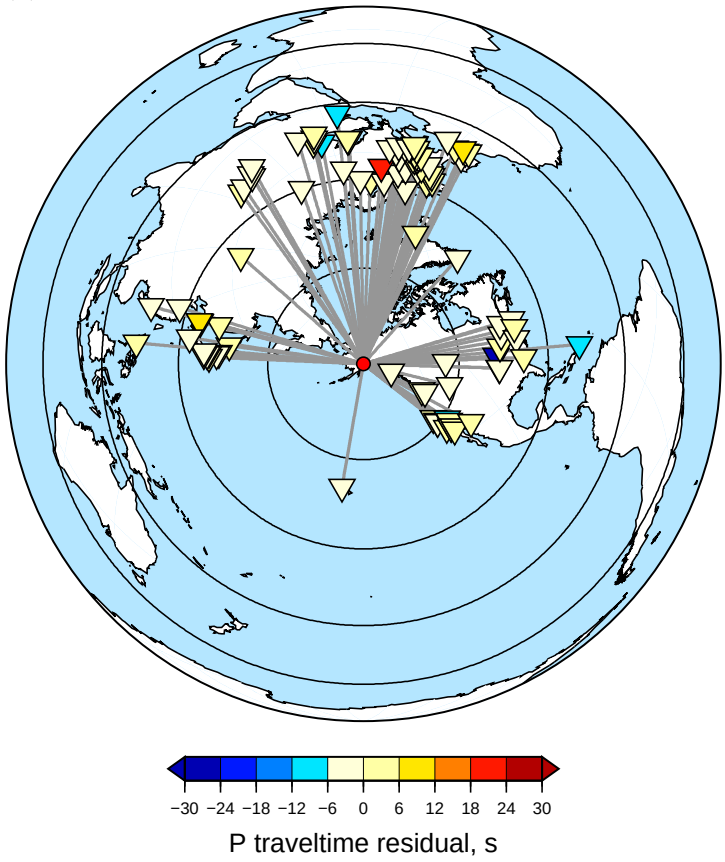

(b)

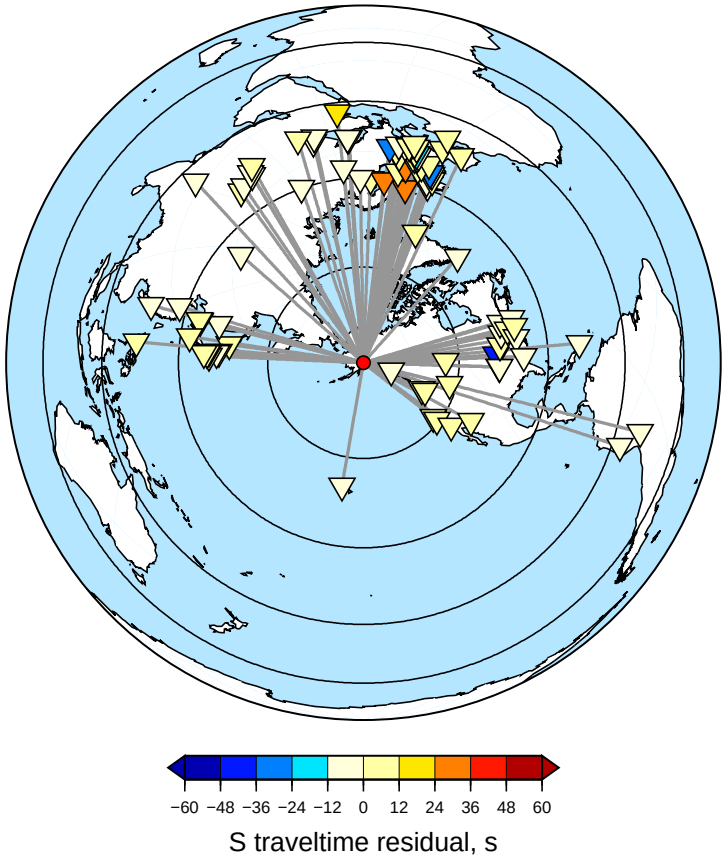

Figure A6: Station coverage of P and S arrival times for event 19340618. The color of each triangle corresponds to the traveltime difference between the observed time and the time predicted using the maximum likelihood hypocenter and origin time, with a 1D Earth model. See also Figure B6.

(a)

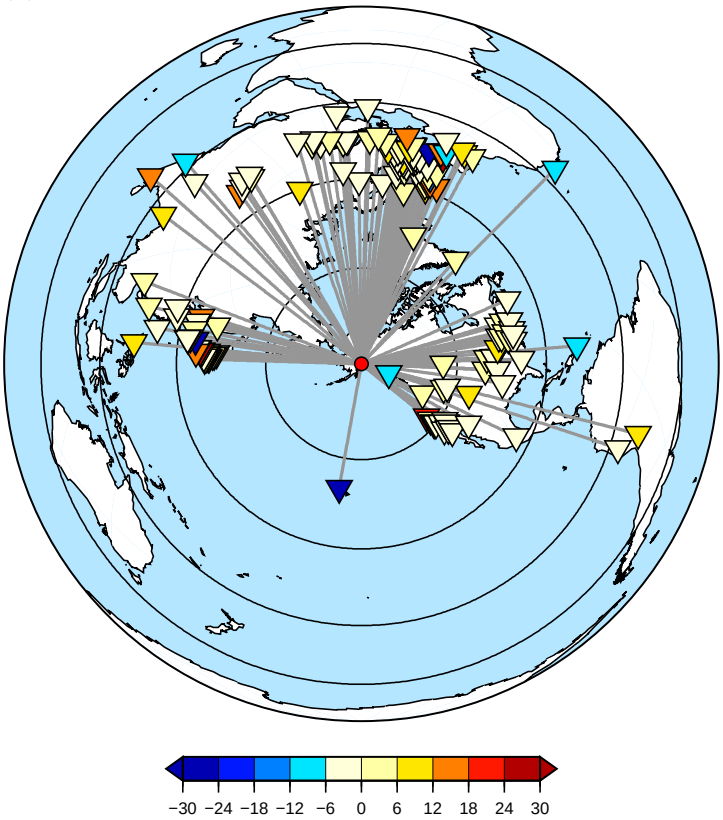

(b)

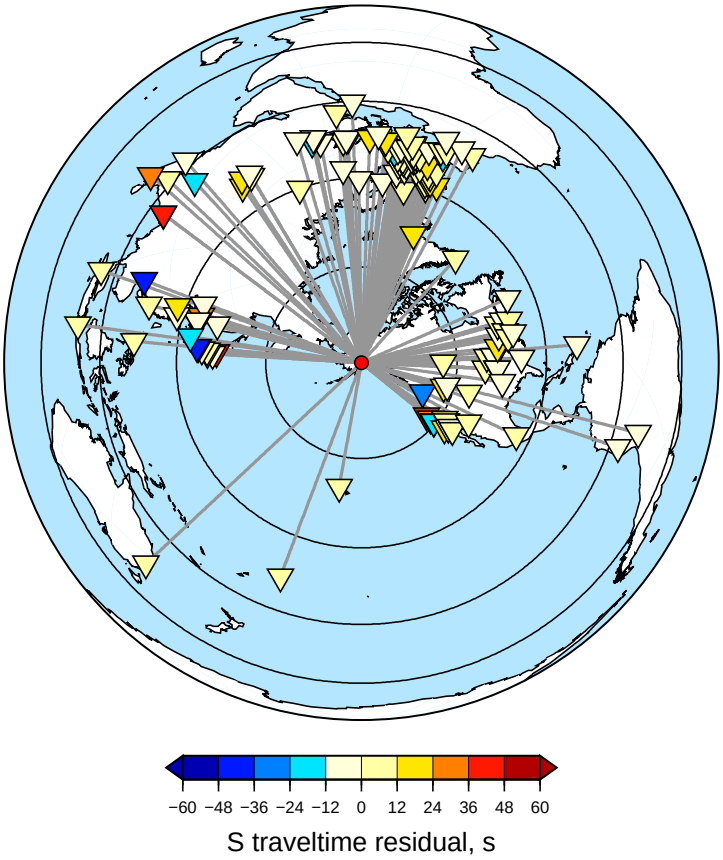

Figure A7: Station coverage of P and S arrival times for event 19361023. The color of each triangle corresponds to the traveltime difference between the observed time and the time predicted using the maximum likelihood hypocenter and origin time, with a 1D Earth model. See also Figure B7.

(a)

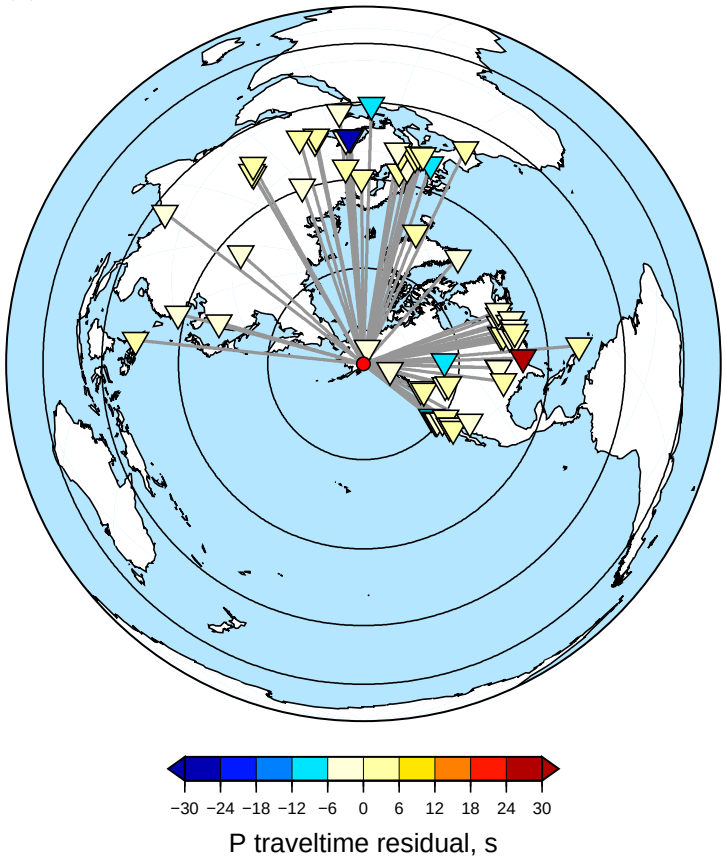

(b)

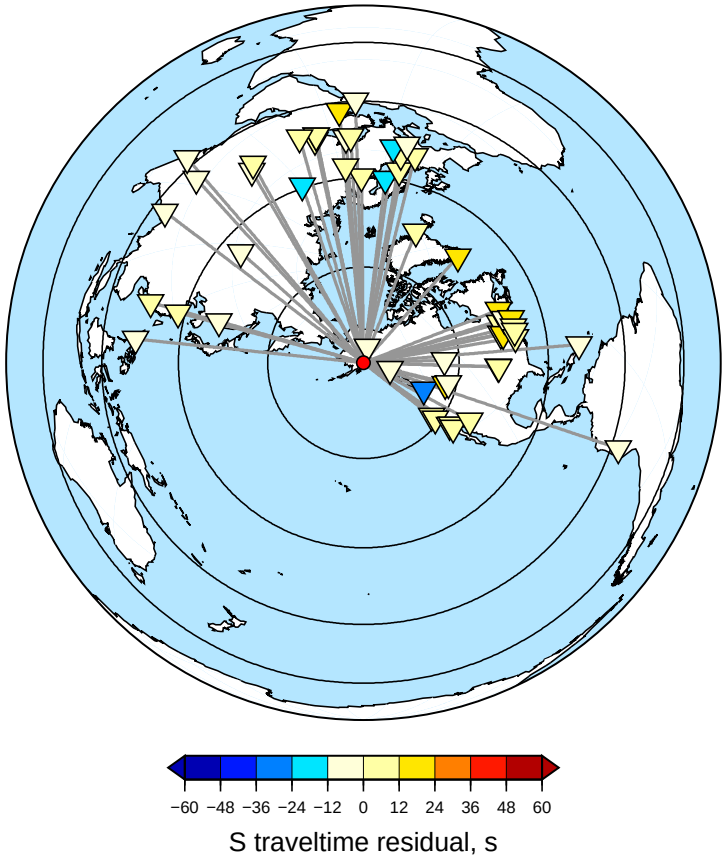

Figure A8: Station coverage of P and S arrival times for event 19371024. The color of each triangle corresponds to the traveltime difference between the observed time and the time predicted using the maximum likelihood hypocenter and origin time, with a 1D Earth model. See also Figure B8.

(a)

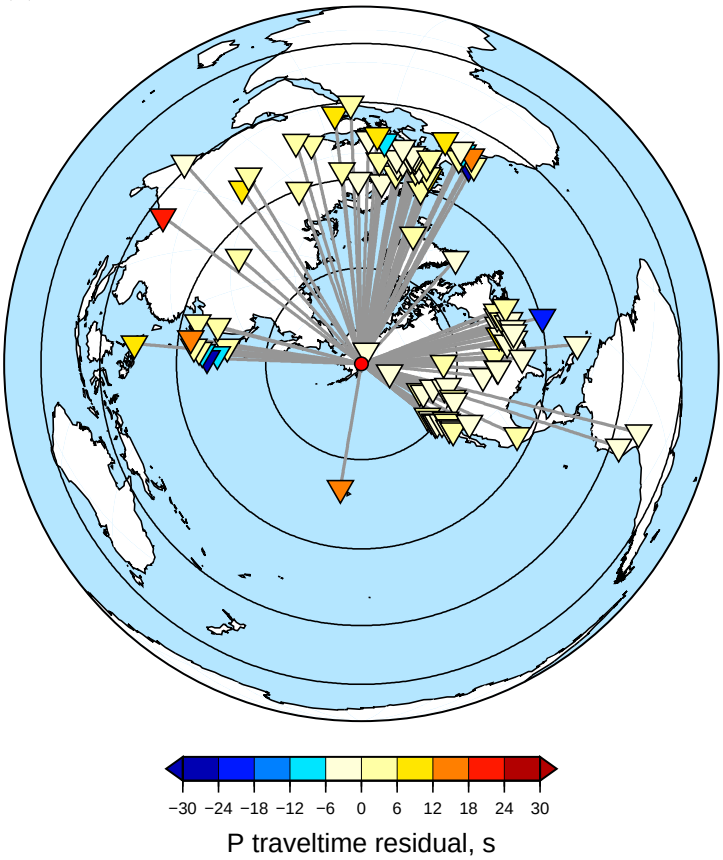

(b)

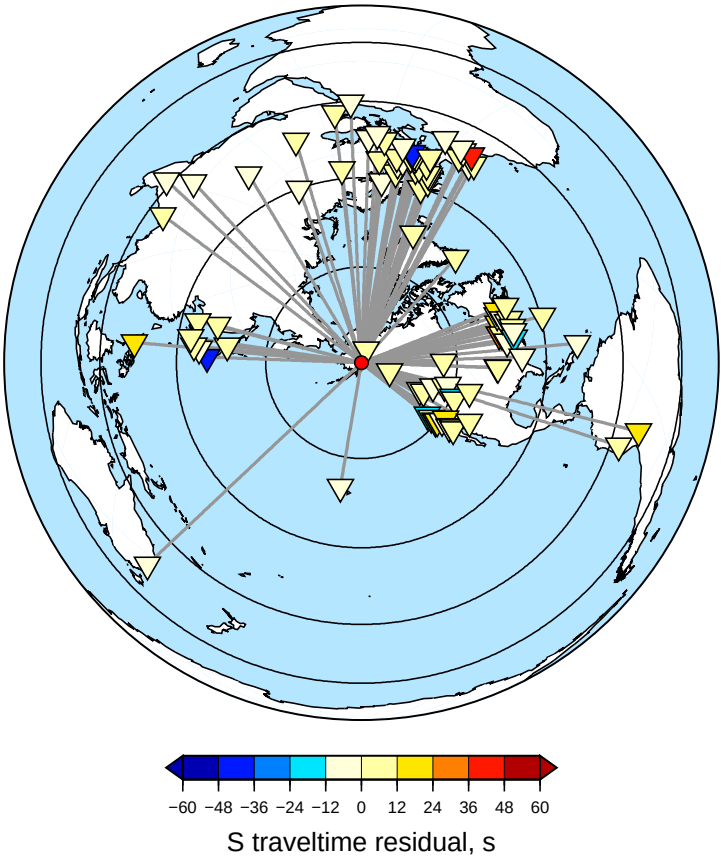

Figure A9: Station coverage of P and S arrival times for event 19410730. The color of each triangle corresponds to the traveltime difference between the observed time and the time predicted using the maximum likelihood hypocenter and origin time, with a 1D Earth model. See also Figure B9.

(a)

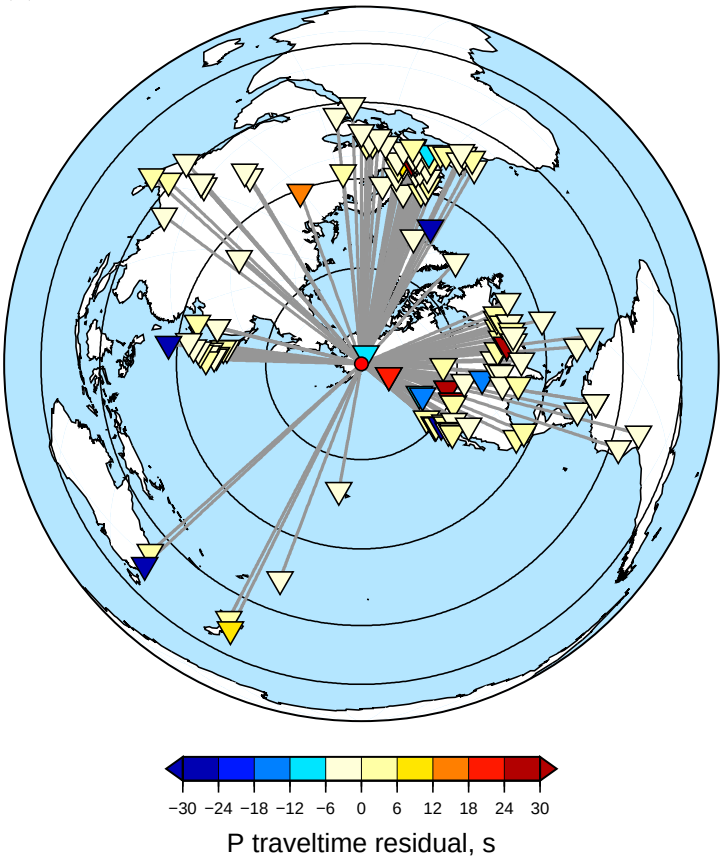

(b)

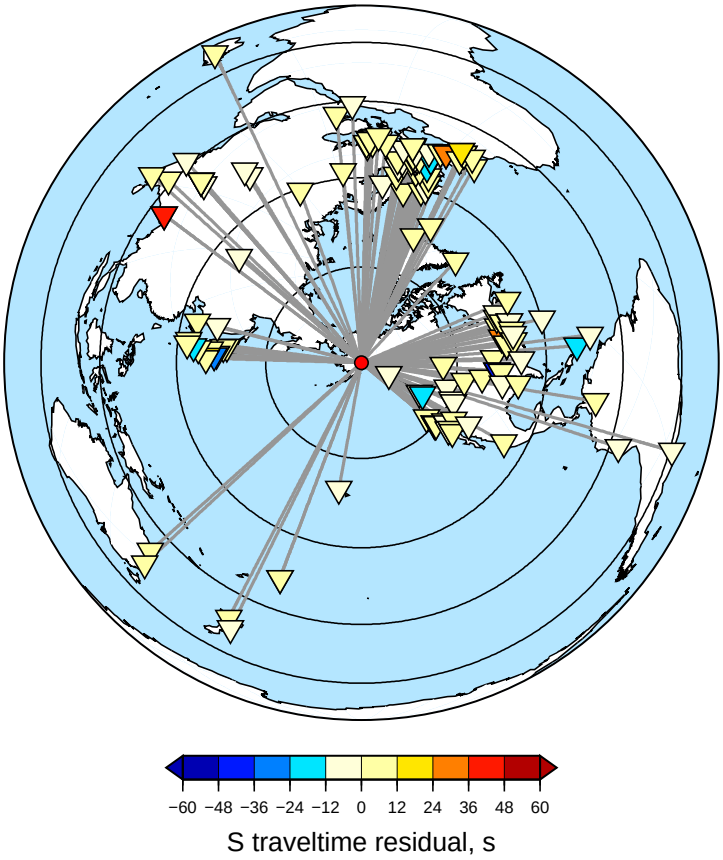

Figure A10: Station coverage of P and S arrival times for event 19431103. The color of each triangle corresponds to the traveltime difference between the observed time and the time predicted using the maximum likelihood hypocenter and origin time, with a 1D Earth model. See also Figure B10.

(a)

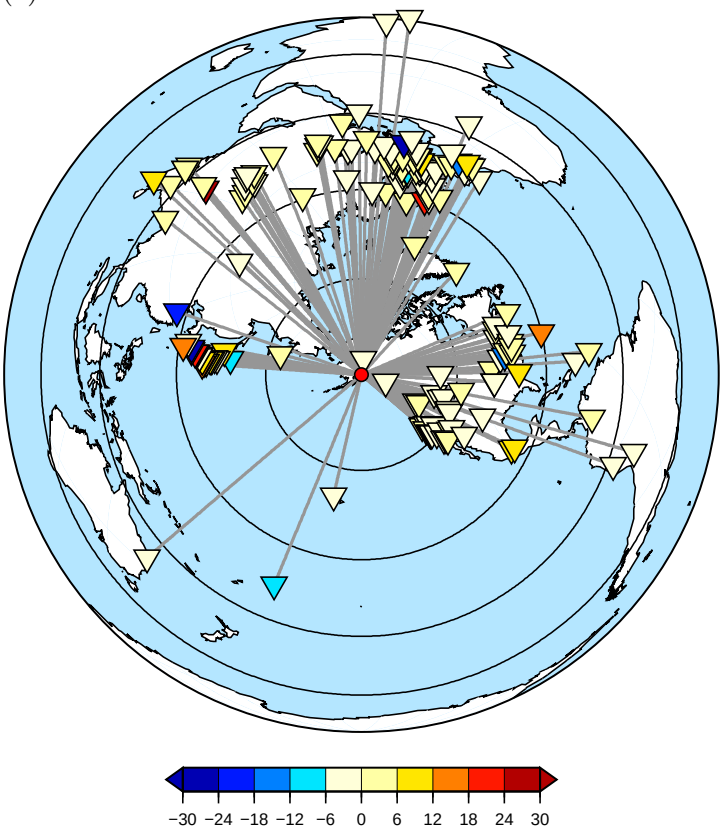

(b)

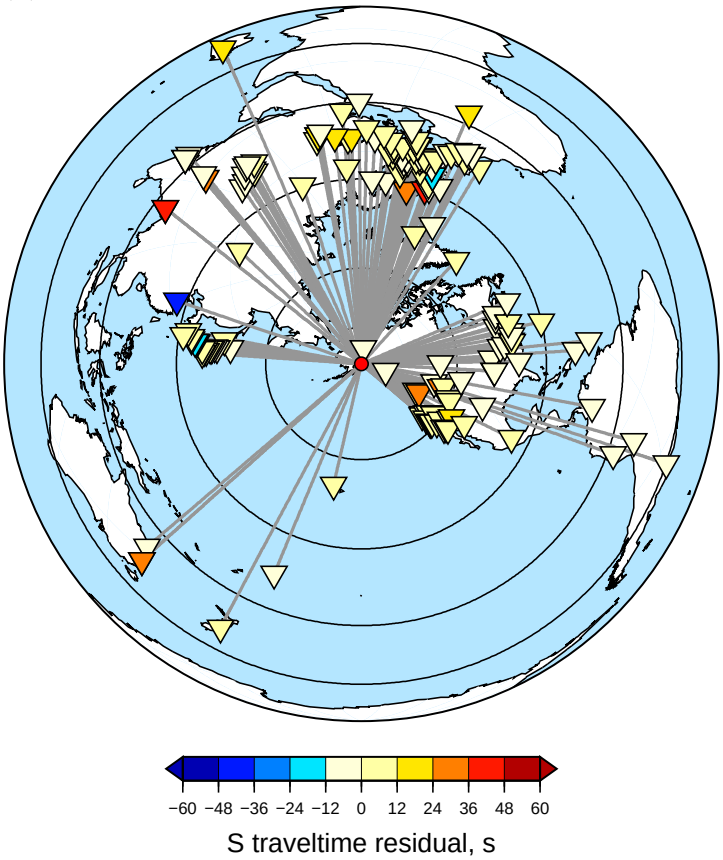

Figure A11: Station coverage of P and S arrival times for event 19490927. The color of each triangle corresponds to the traveltime difference between the observed time and the time predicted using the maximum likelihood hypocenter and origin time, with a 1D Earth model. See also Figure B11.

(a)

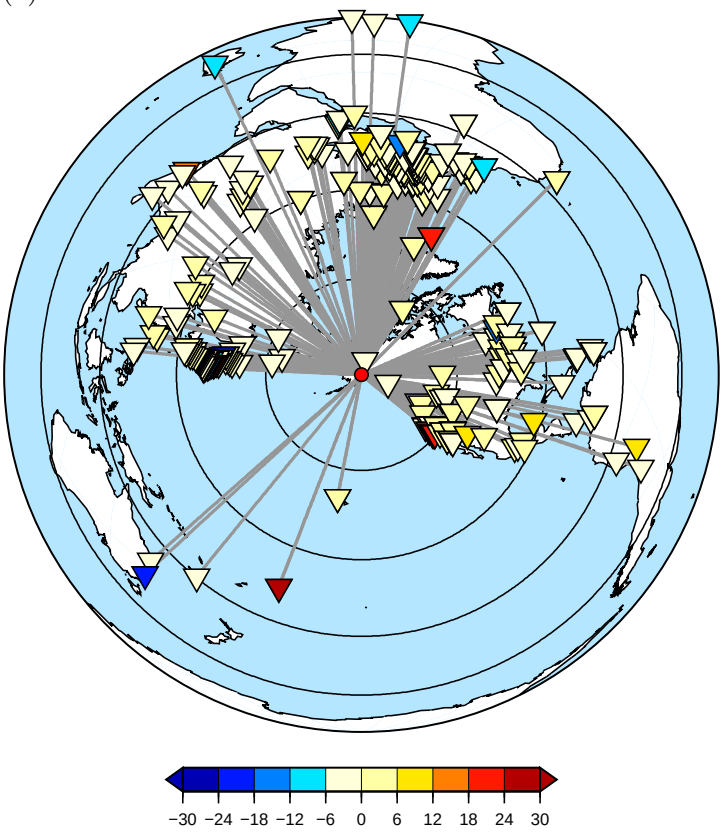

(b)

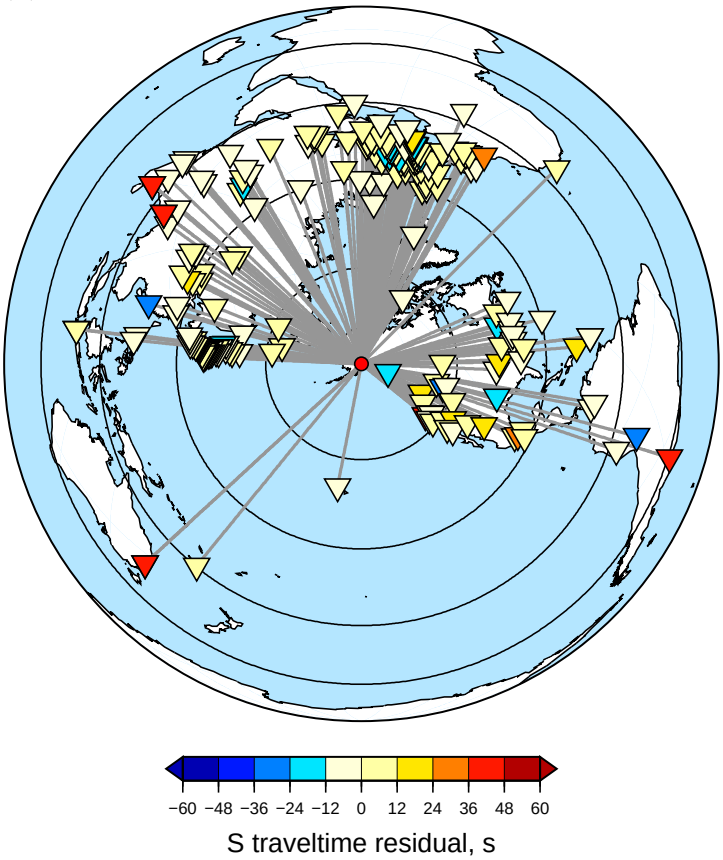

Figure A12: Station coverage of P and S arrival times for event 19541003. The color of each triangle corresponds to the traveltime difference between the observed time and the time predicted using the maximum likelihood hypocenter and origin time, with a 1D Earth model. See also Figure B12.

(a)

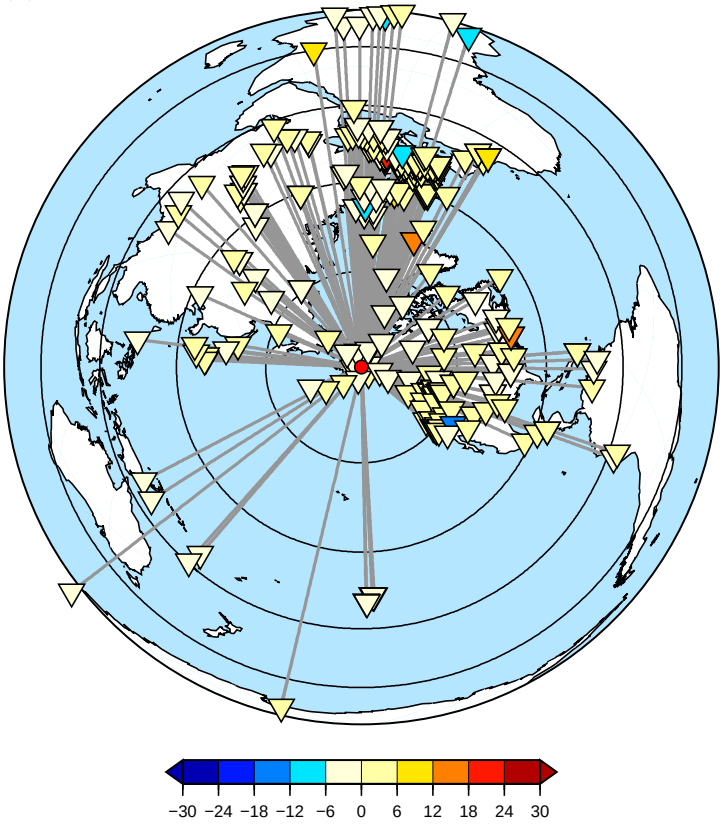

(b)

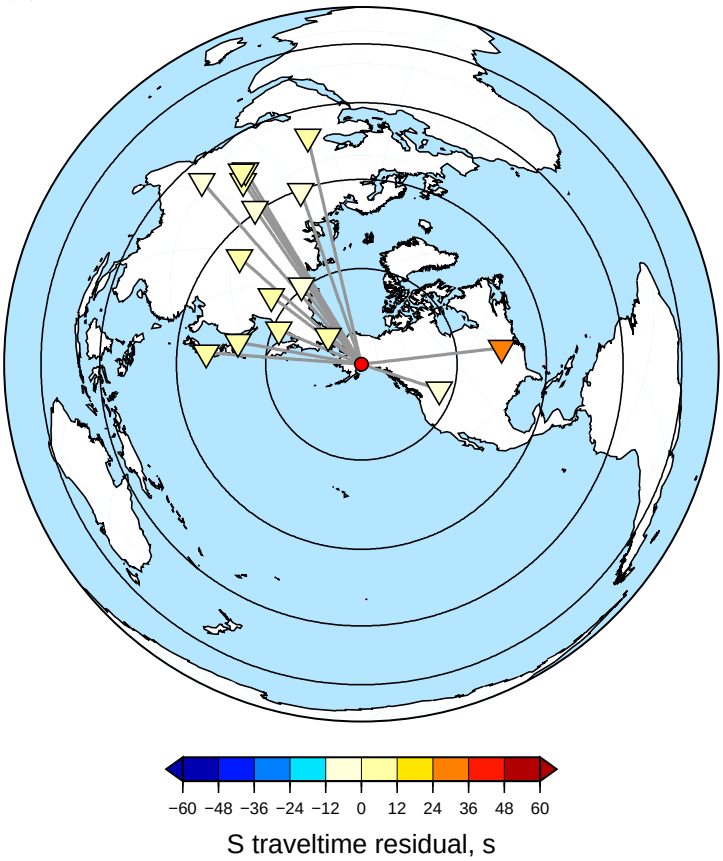

Figure A13: Station coverage of P and S arrival times for event 19741229. The color of each triangle corresponds to the traveltime difference between the observed time and the time predicted using the maximum likelihood hypocenter and origin time, with a 1D Earth model. See also Figure B13.

(a)

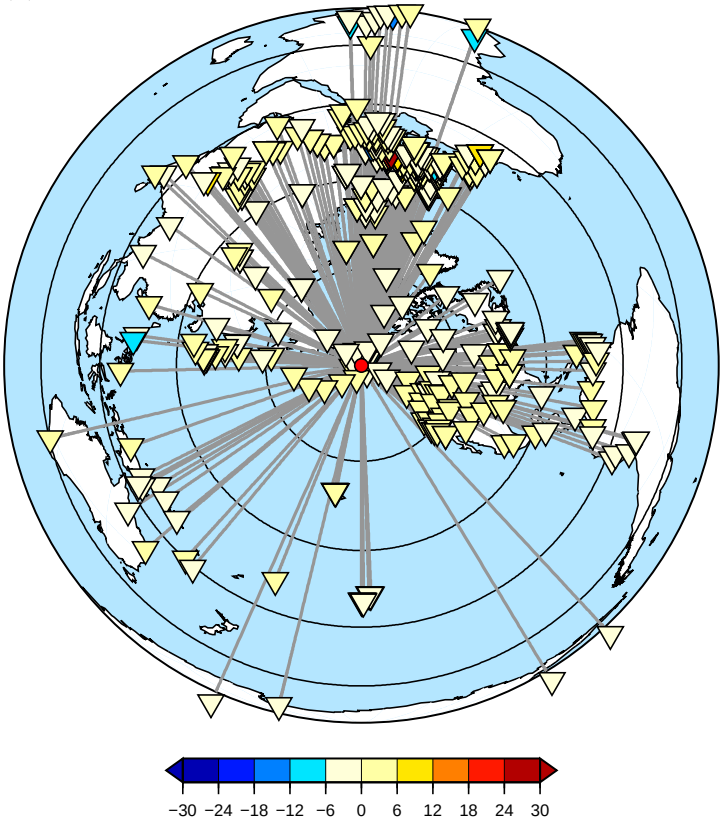

(b)

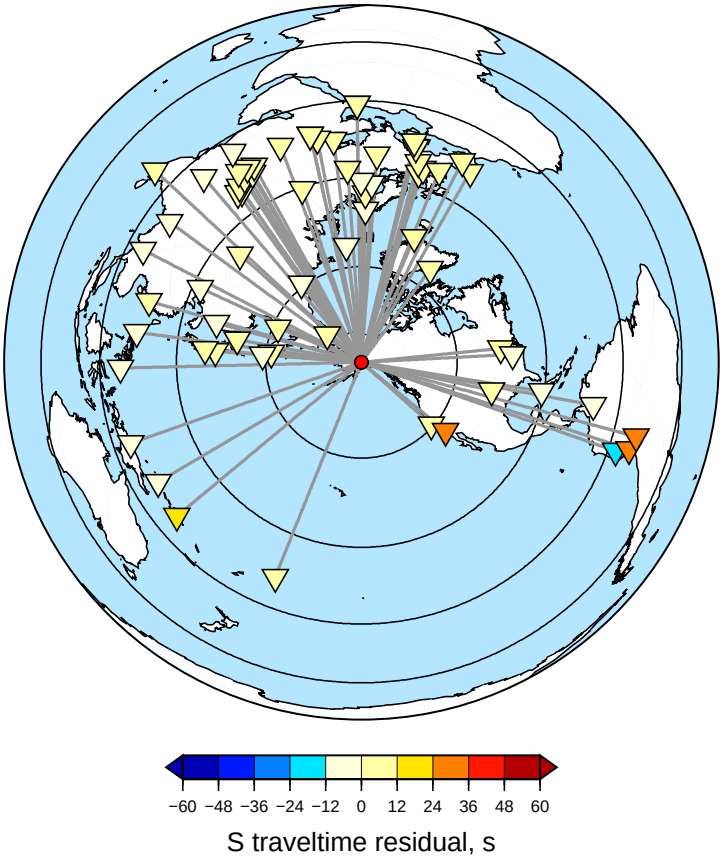

Figure A14: Station coverage of P and S arrival times for event 19750101. The color of each triangle corresponds to the traveltime difference between the observed time and the time predicted using the maximum likelihood hypocenter and origin time, with a 1D Earth model. See also Figure B14.

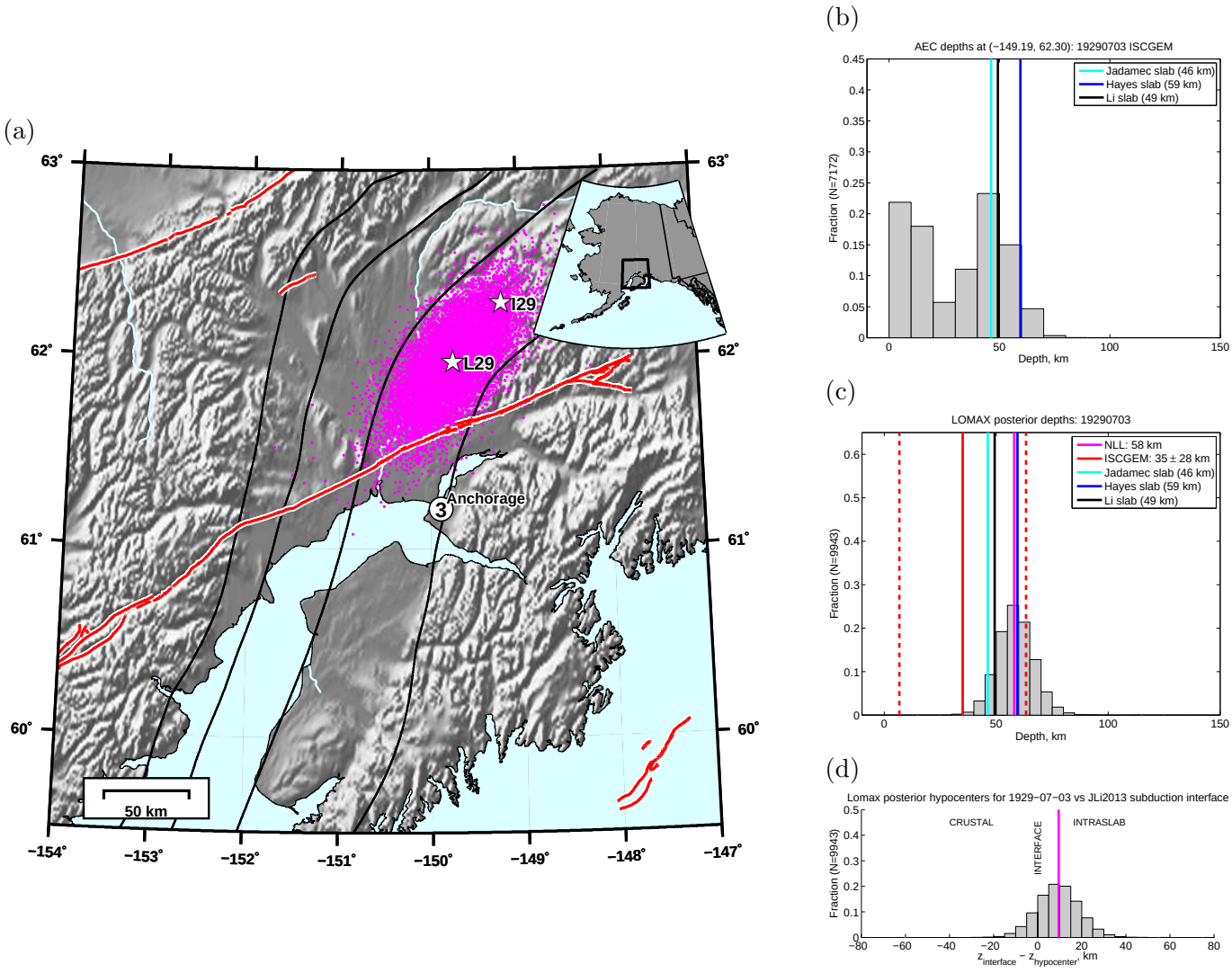

Figure B1: Event page for 19290703. See station coverage in Figure A1. (a) Posterior epicenters from NonLinLoc (*Lomax et al.*, 2000, 2014), with the star representing the maximum likelihood epicenter. Also shown are felt reports from *Brockman et al.* (1988). (b) Distribution of depths for modern seismicity (2000-01-01 to 2018-01-01, $M \geq 0$) within 40 km of the ISC-GEM epicenter. Also shown, for three subduction interface geometries, is the subduction interface depth at the ISC-GEM epicenter. The number of earthquakes in the distribution is labeled on the y-axis. (c) Distribution of depths for posterior hypocenters. Also shown are the depth estimates from NonLinLoc, ISC-GEM, and *Doser and Brown* (2001). The number of posterior hypocenters is labeles on the y-axis. (d) Distribution of the depth differences between the subduction interface, evaluated at the posterior epicenters, and the posterior hypocenters in (c).

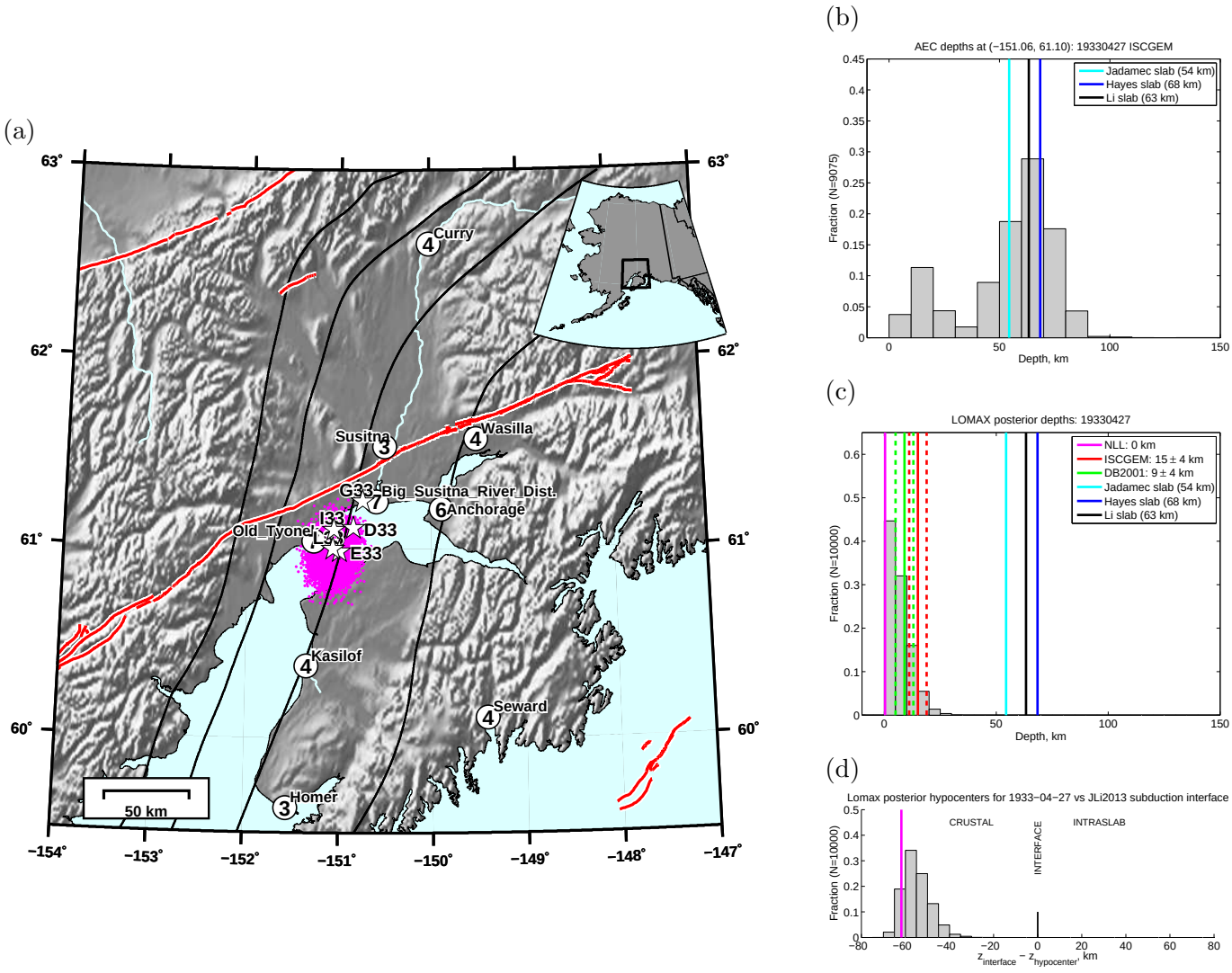

Figure B2: Event page for 19330427. See station coverage in Figure A2. (a) Posterior epicenters from NonLinLoc (*Lomax et al.*, 2000, 2014), with the star representing the maximum likelihood epicenter. Also shown are felt reports from *Brockman et al.* (1988). (b) Distribution of depths for modern seismicity (2000-01-01 to 2018-01-01, $M \geq 0$) within 40 km of the ISC-GEM epicenter. Also shown, for three subduction interface geometries, is the subduction interface depth at the ISC-GEM epicenter. The number of earthquakes in the distribution is labeled on the y-axis. (c) Distribution of depths for posterior hypocenters. Also shown are the depth estimates from NonLinLoc, ISC-GEM, and *Doser and Brown* (2001). The number of posterior hypocenters is labeles on the y-axis. (d) Distribution of the depth differences between the subduction interface, evaluated at the posterior epicenters, and the posterior hypocenters in (c).

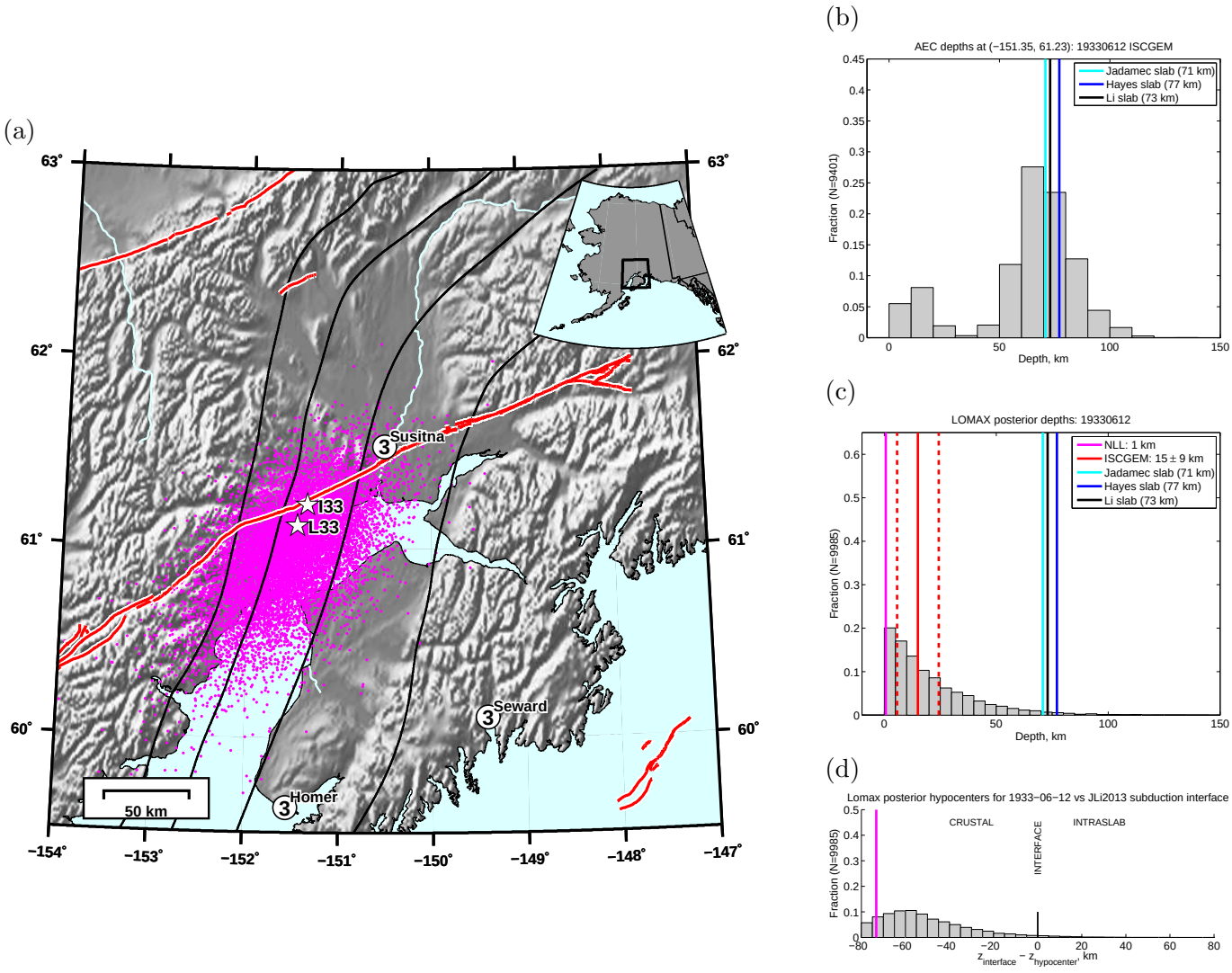

Figure B3: Event page for 19330612. See station coverage in Figure A3. (a) Posterior epicenters from NonLinLoc (*Lomax et al.*, 2000, 2014), with the star representing the maximum likelihood epicenter. Also shown are felt reports from *Brockman et al.* (1988). (b) Distribution of depths for modern seismicity (2000-01-01 to 2018-01-01, $M \geq 0$) within 40 km of the ISC-GEM epicenter. Also shown, for three subduction interface geometries, is the subduction interface depth at the ISC-GEM epicenter. The number of earthquakes in the distribution is labeled on the y-axis. (c) Distribution of depths for posterior hypocenters. Also shown are the depth estimates from NonLinLoc, ISC-GEM, and *Doser and Brown* (2001). The number of posterior hypocenters is labeles on the y-axis. (d) Distribution of the depth differences between the subduction interface, evaluated at the posterior epicenters, and the posterior hypocenters in (c).

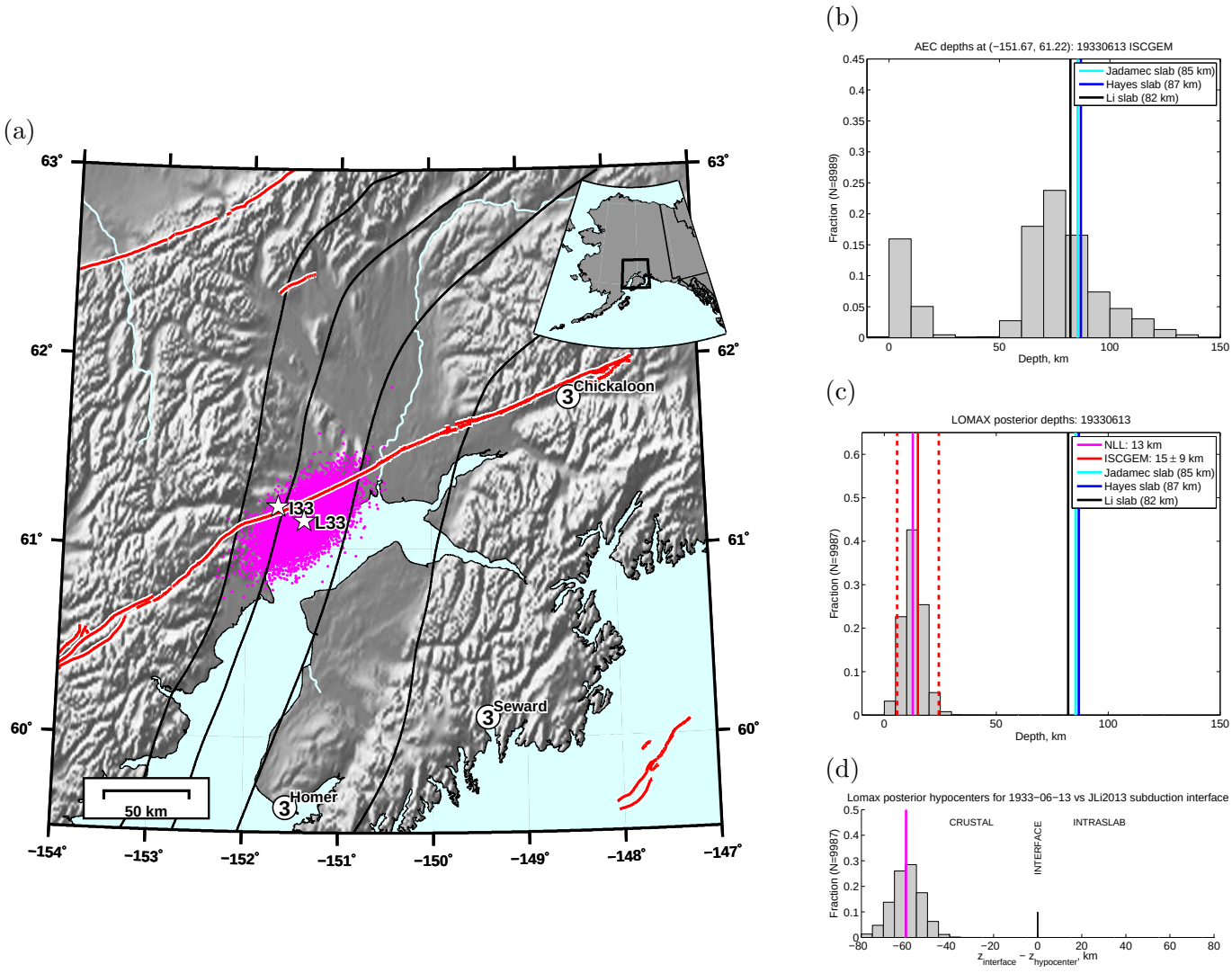

Figure B4: Event page for 19330613. See station coverage in Figure A4. (a) Posterior epicenters from NonLinLoc (*Lomax et al.*, 2000, 2014), with the star representing the maximum likelihood epicenter. Also shown are felt reports from *Brockman et al.* (1988). (b) Distribution of depths for modern seismicity (2000-01-01 to 2018-01-01, $M \geq 0$) within 40 km of the ISC-GEM epicenter. Also shown, for three subduction interface geometries, is the subduction interface depth at the ISC-GEM epicenter. The number of earthquakes in the distribution is labeled on the y-axis. (c) Distribution of depths for posterior hypocenters. Also shown are the depth estimates from NonLinLoc, ISC-GEM, and *Doser and Brown* (2001). The number of posterior hypocenters is labeles on the y-axis. (d) Distribution of the depth differences between the subduction interface, evaluated at the posterior epicenters, and the posterior hypocenters in (c).

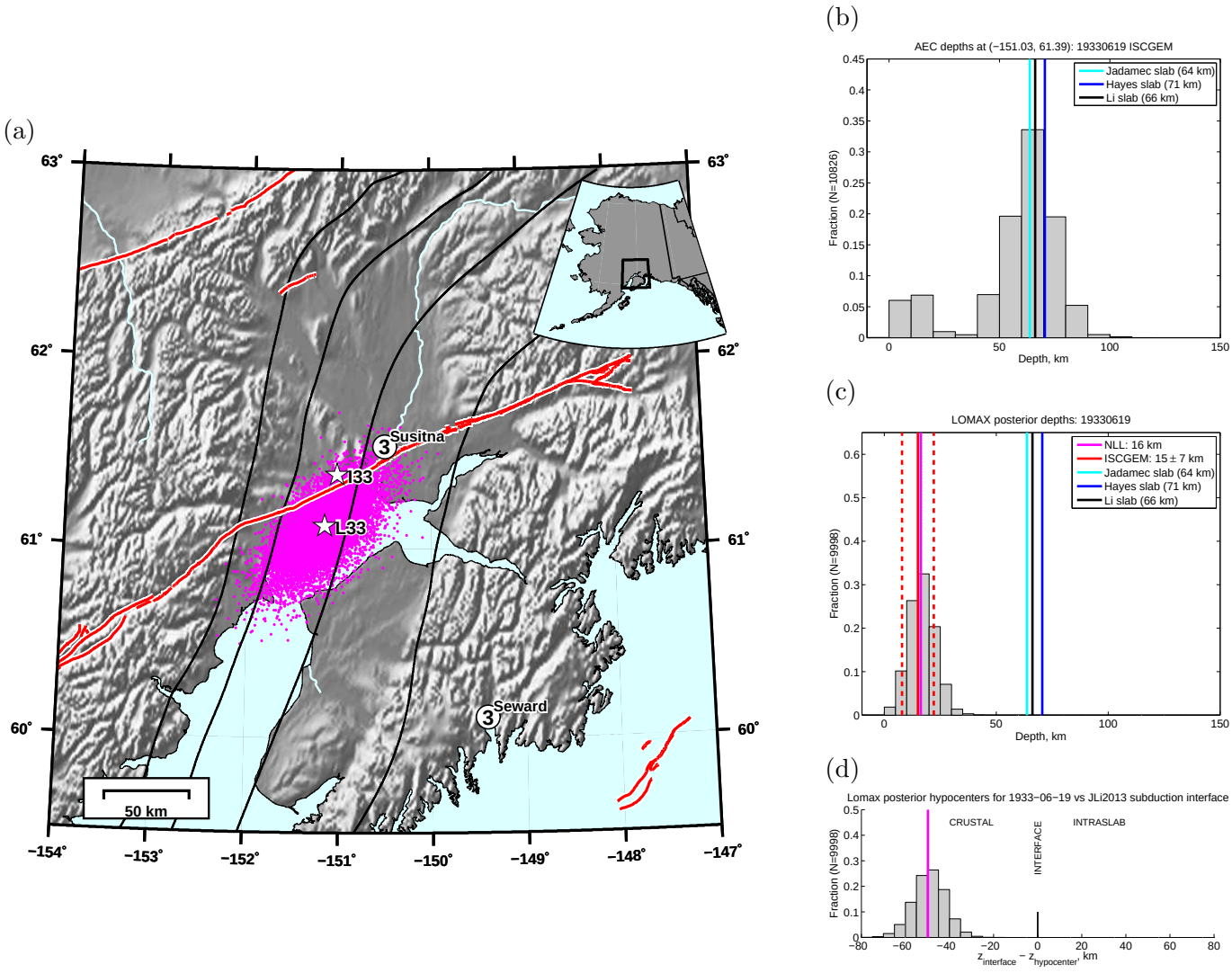

Figure B5: Event page for 19330619. See station coverage in Figure A5. (a) Posterior epicenters from NonLinLoc (*Lomax et al.*, 2000, 2014), with the star representing the maximum likelihood epicenter. Also shown are felt reports from *Brockman et al.* (1988). (b) Distribution of depths for modern seismicity (2000-01-01 to 2018-01-01, $M \geq 0$) within 40 km of the ISC-GEM epicenter. Also shown, for three subduction interface geometries, is the subduction interface depth at the ISC-GEM epicenter. The number of earthquakes in the distribution is labeled on the y-axis. (c) Distribution of depths for posterior hypocenters. Also shown are the depth estimates from NonLinLoc, ISC-GEM, and *Doser and Brown* (2001). The number of posterior hypocenters is labeles on the y-axis. (d) Distribution of the depth differences between the subduction interface, evaluated at the posterior epicenters, and the posterior hypocenters in (c).

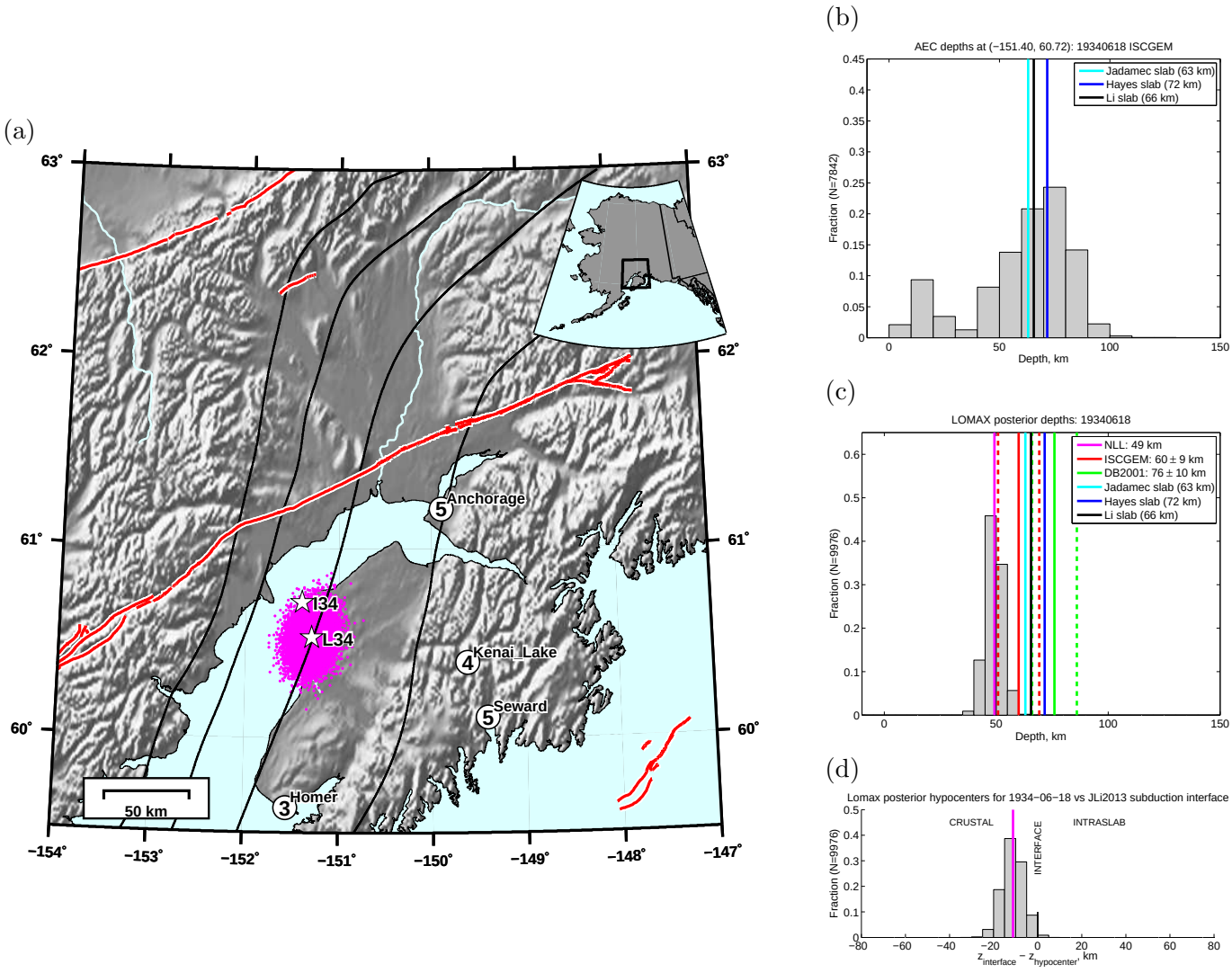

Figure B6: Event page for 19340618. See station coverage in Figure A6. (a) Posterior epicenters from NonLinLoc (*Lomax et al.*, 2000, 2014), with the star representing the maximum likelihood epicenter. Also shown are felt reports from *Brockman et al.* (1988). (b) Distribution of depths for modern seismicity (2000-01-01 to 2018-01-01, $M \geq 0$) within 40 km of the ISC-GEM epicenter. Also shown, for three subduction interface geometries, is the subduction interface depth at the ISC-GEM epicenter. The number of earthquakes in the distribution is labeled on the y-axis. (c) Distribution of depths for posterior hypocenters. Also shown are the depth estimates from NonLinLoc, ISC-GEM, and *Doser and Brown* (2001). The number of posterior hypocenters is labeles on the y-axis. (d) Distribution of the depth differences between the subduction interface, evaluated at the posterior epicenters, and the posterior hypocenters in (c).

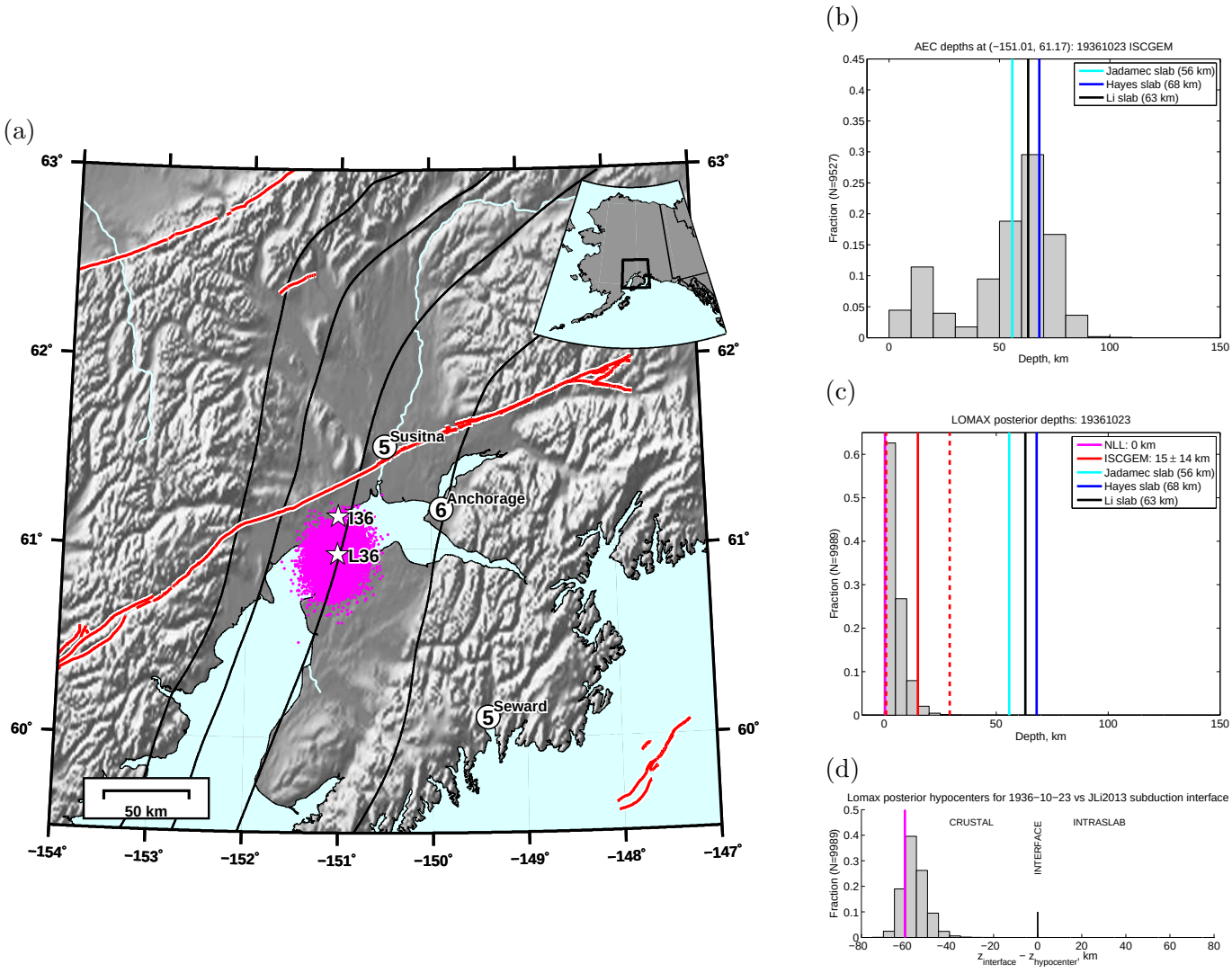

Figure B7: Event page for 19361023. See station coverage in Figure A7. (a) Posterior epicenters from NonLinLoc (*Lomax et al.*, 2000, 2014), with the star representing the maximum likelihood epicenter. Also shown are felt reports from *Brockman et al.* (1988). (b) Distribution of depths for modern seismicity (2000-01-01 to 2018-01-01, $M \geq 0$) within 40 km of the ISC-GEM epicenter. Also shown, for three subduction interface geometries, is the subduction interface depth at the ISC-GEM epicenter. The number of earthquakes in the distribution is labeled on the y-axis. (c) Distribution of depths for posterior hypocenters. Also shown are the depth estimates from NonLinLoc, ISC-GEM, and *Doser and Brown* (2001). The number of posterior hypocenters is labeles on the y-axis. (d) Distribution of the depth differences between the subduction interface, evaluated at the posterior epicenters, and the posterior hypocenters in (c).

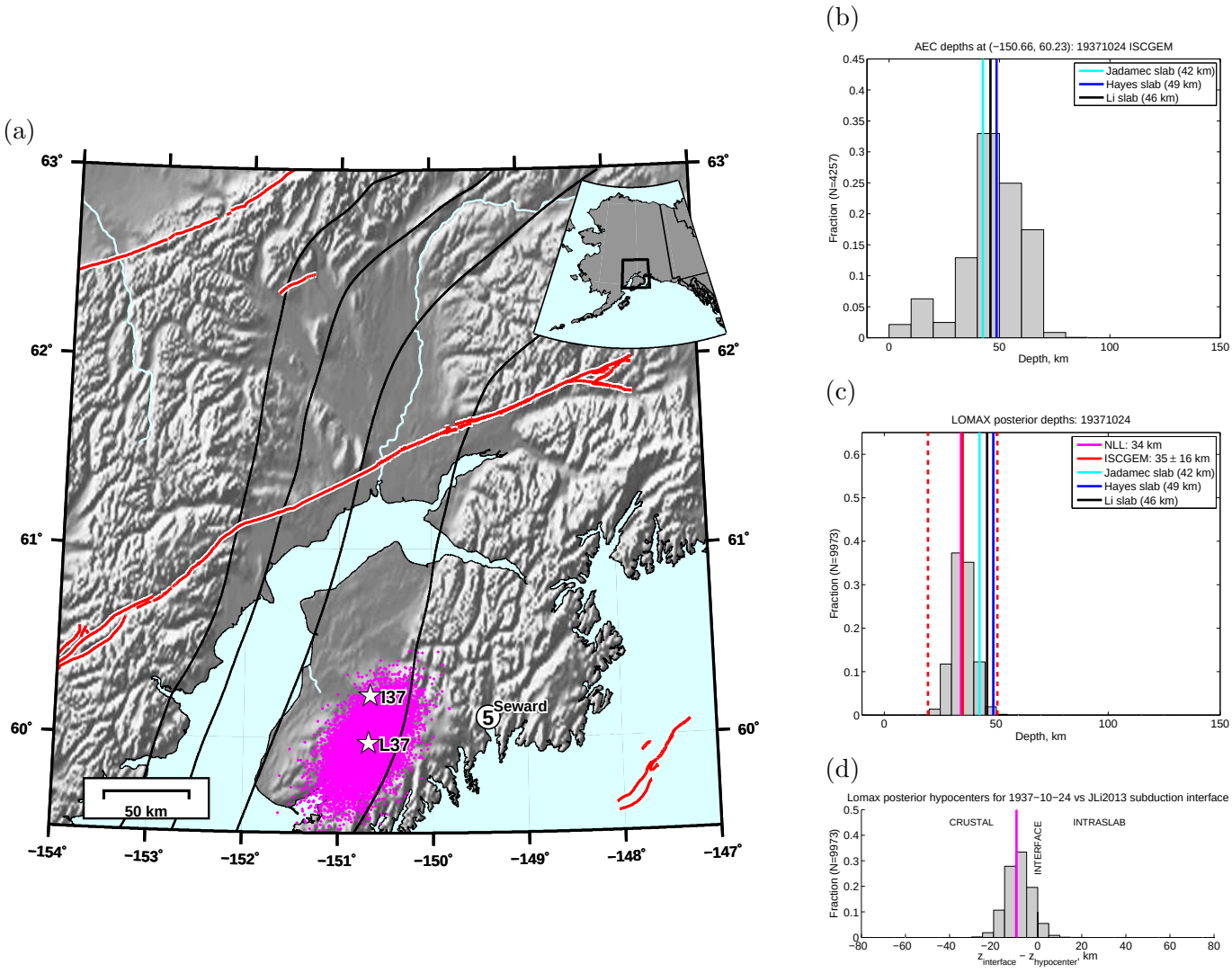

Figure B8: Event page for 19371024. See station coverage in Figure A8. (a) Posterior epicenters from NonLinLoc (*Lomax et al.*, 2000, 2014), with the star representing the maximum likelihood epicenter. Also shown are felt reports from *Brockman et al.* (1988). (b) Distribution of depths for modern seismicity (2000-01-01 to 2018-01-01, $M \geq 0$) within 40 km of the ISC-GEM epicenter. Also shown, for three subduction interface geometries, is the subduction interface depth at the ISC-GEM epicenter. The number of earthquakes in the distribution is labeled on the y-axis. (c) Distribution of depths for posterior hypocenters. Also shown are the depth estimates from NonLinLoc, ISC-GEM, and *Doser and Brown* (2001). The number of posterior hypocenters is labeles on the y-axis. (d) Distribution of the depth differences between the subduction interface, evaluated at the posterior epicenters, and the posterior hypocenters in (c).

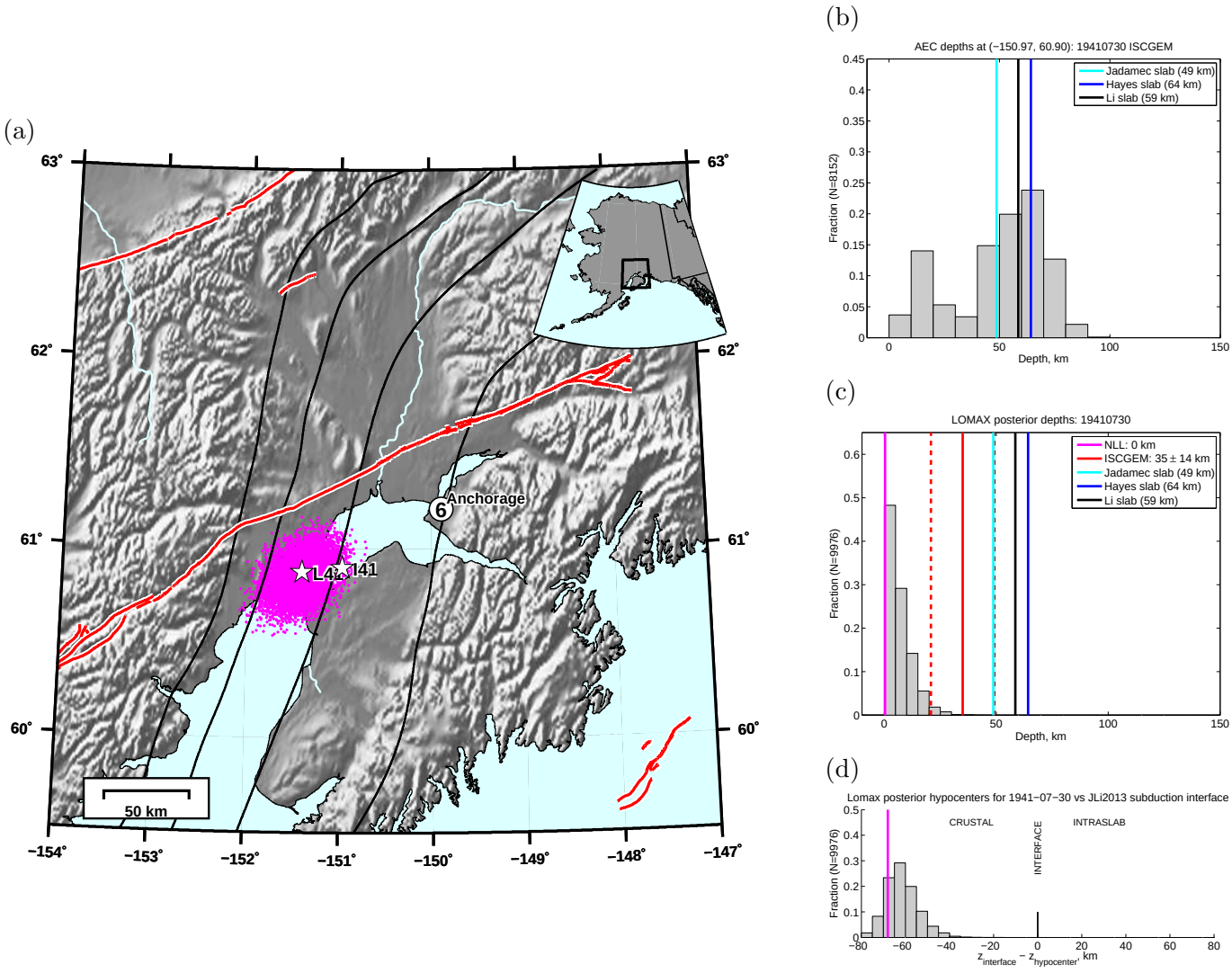

Figure B9: Event page for 19410730. See station coverage in Figure A9. (a) Posterior epicenters from NonLinLoc (*Lomax et al.*, 2000, 2014), with the star representing the maximum likelihood epicenter. Also shown are felt reports from *Brockman et al.* (1988). (b) Distribution of depths for modern seismicity (2000-01-01 to 2018-01-01, $M \geq 0$) within 40 km of the ISC-GEM epicenter. Also shown, for three subduction interface geometries, is the subduction interface depth at the ISC-GEM epicenter. The number of earthquakes in the distribution is labeled on the y-axis. (c) Distribution of depths for posterior hypocenters. Also shown are the depth estimates from NonLinLoc, ISC-GEM, and *Doser and Brown* (2001). The number of posterior hypocenters is labeles on the y-axis. (d) Distribution of the depth differences between the subduction interface, evaluated at the posterior epicenters, and the posterior hypocenters in (c).

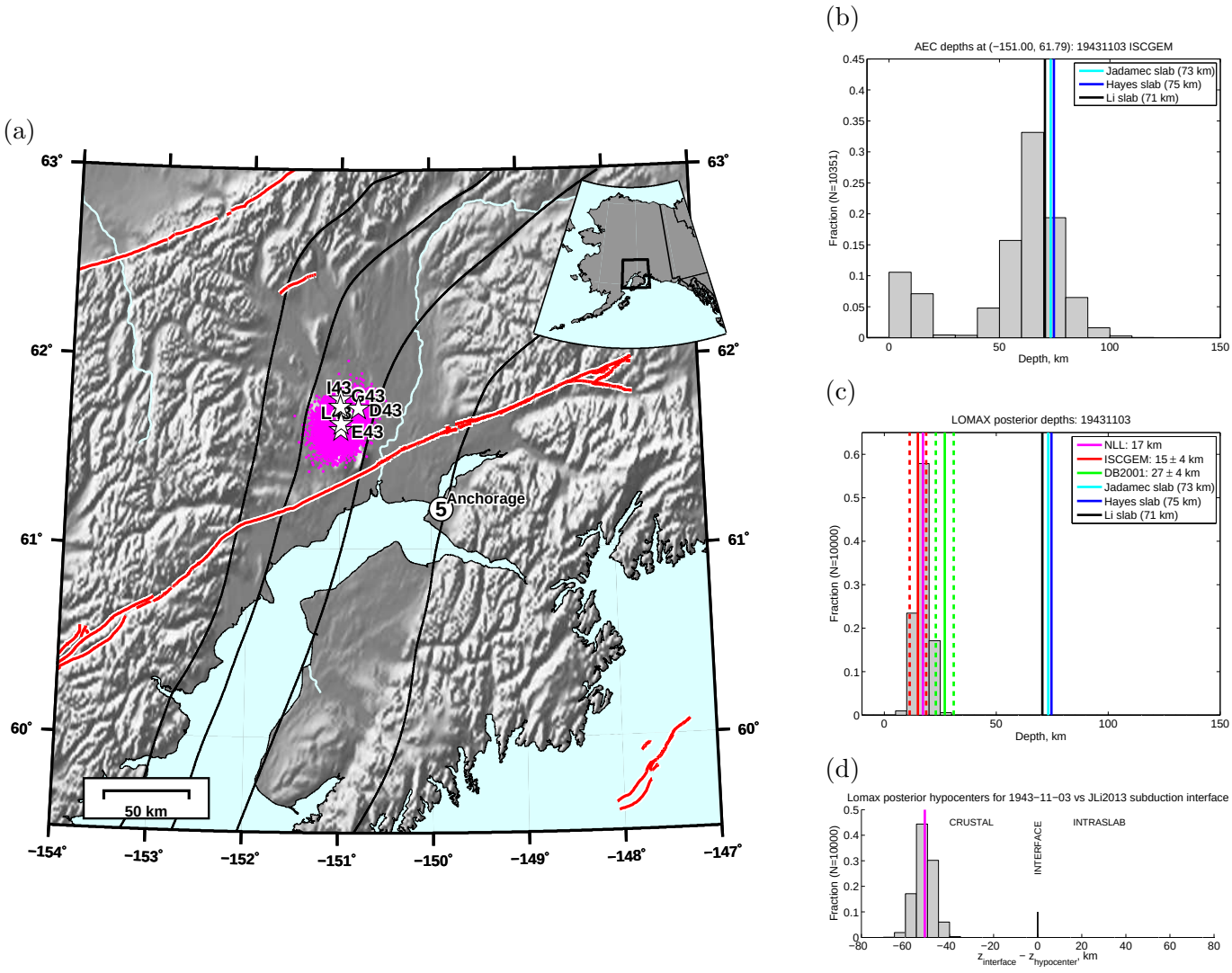

Figure B10: Event page for 19431103. See station coverage in Figure A10. (a) Posterior epicenters from NonLinLoc (*Lomax et al.*, 2000, 2014), with the star representing the maximum likelihood epicenter. Also shown are felt reports from *Brockman et al.* (1988). (b) Distribution of depths for modern seismicity (2000-01-01 to 2018-01-01, $M \geq 0$) within 40 km of the ISC-GEM epicenter. Also shown, for three subduction interface geometries, is the subduction interface depth at the ISC-GEM epicenter. The number of earthquakes in the distribution is labeled on the y-axis. (c) Distribution of depths for posterior hypocenters. Also shown are the depth estimates from NonLinLoc, ISC-GEM, and *Doser and Brown* (2001). The number of posterior hypocenters is labeles on the y-axis. (d) Distribution of the depth differences between the subduction interface, evaluated at the posterior epicenters, and the posterior hypocenters in (c).

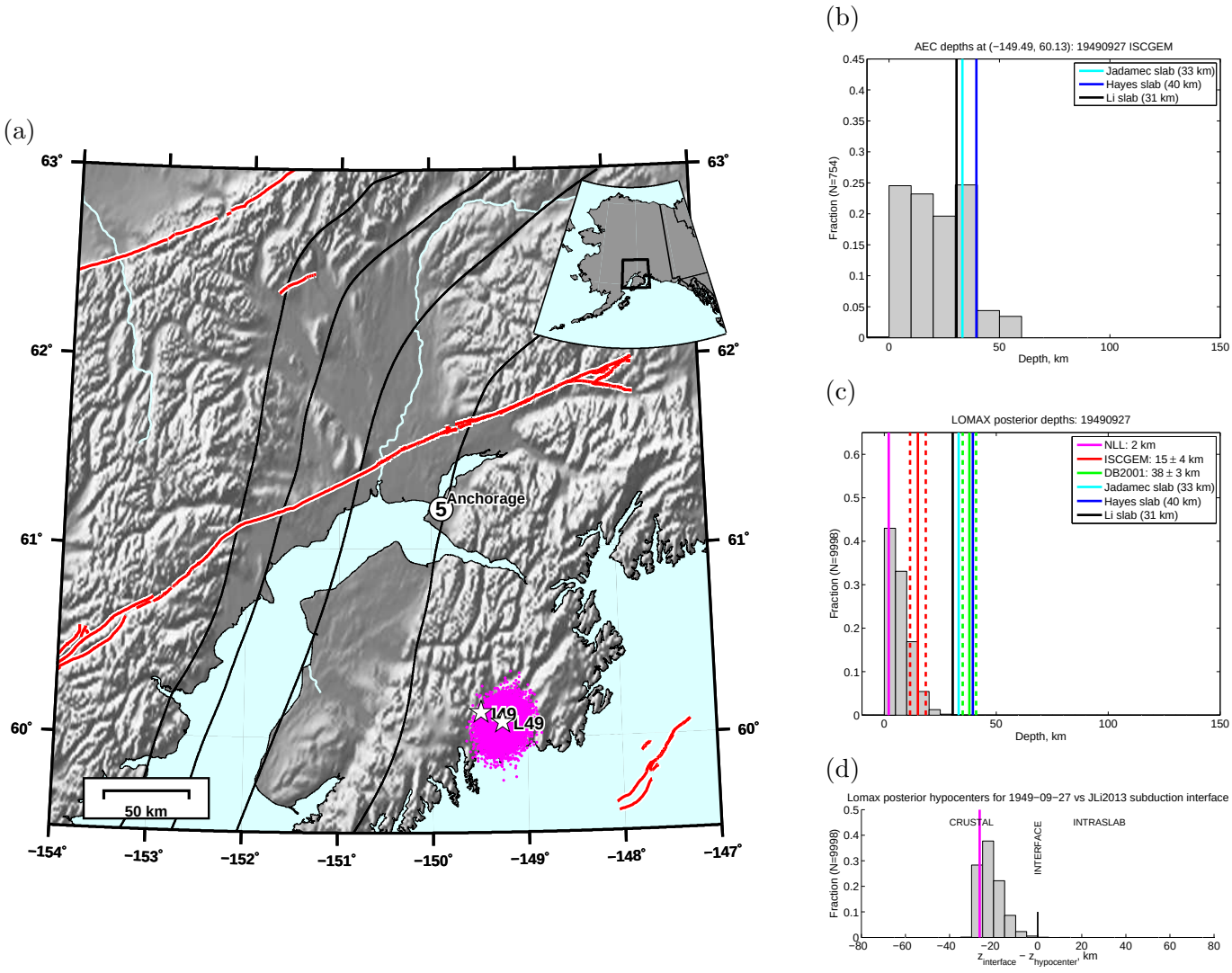

Figure B11: Event page for 19490927. See station coverage in Figure A11. (a) Posterior epicenters from NonLinLoc (*Lomax et al.*, 2000, 2014), with the star representing the maximum likelihood epicenter. Also shown are felt reports from *Brockman et al.* (1988). (b) Distribution of depths for modern seismicity (2000-01-01 to 2018-01-01, $M \geq 0$) within 40 km of the ISC-GEM epicenter. Also shown, for three subduction interface geometries, is the subduction interface depth at the ISC-GEM epicenter. The number of earthquakes in the distribution is labeled on the y-axis. (c) Distribution of depths for posterior hypocenters. Also shown are the depth estimates from NonLinLoc, ISC-GEM, and *Doser and Brown* (2001). The number of posterior hypocenters is labeles on the y-axis. (d) Distribution of the depth differences between the subduction interface, evaluated at the posterior epicenters, and the posterior hypocenters in (c).

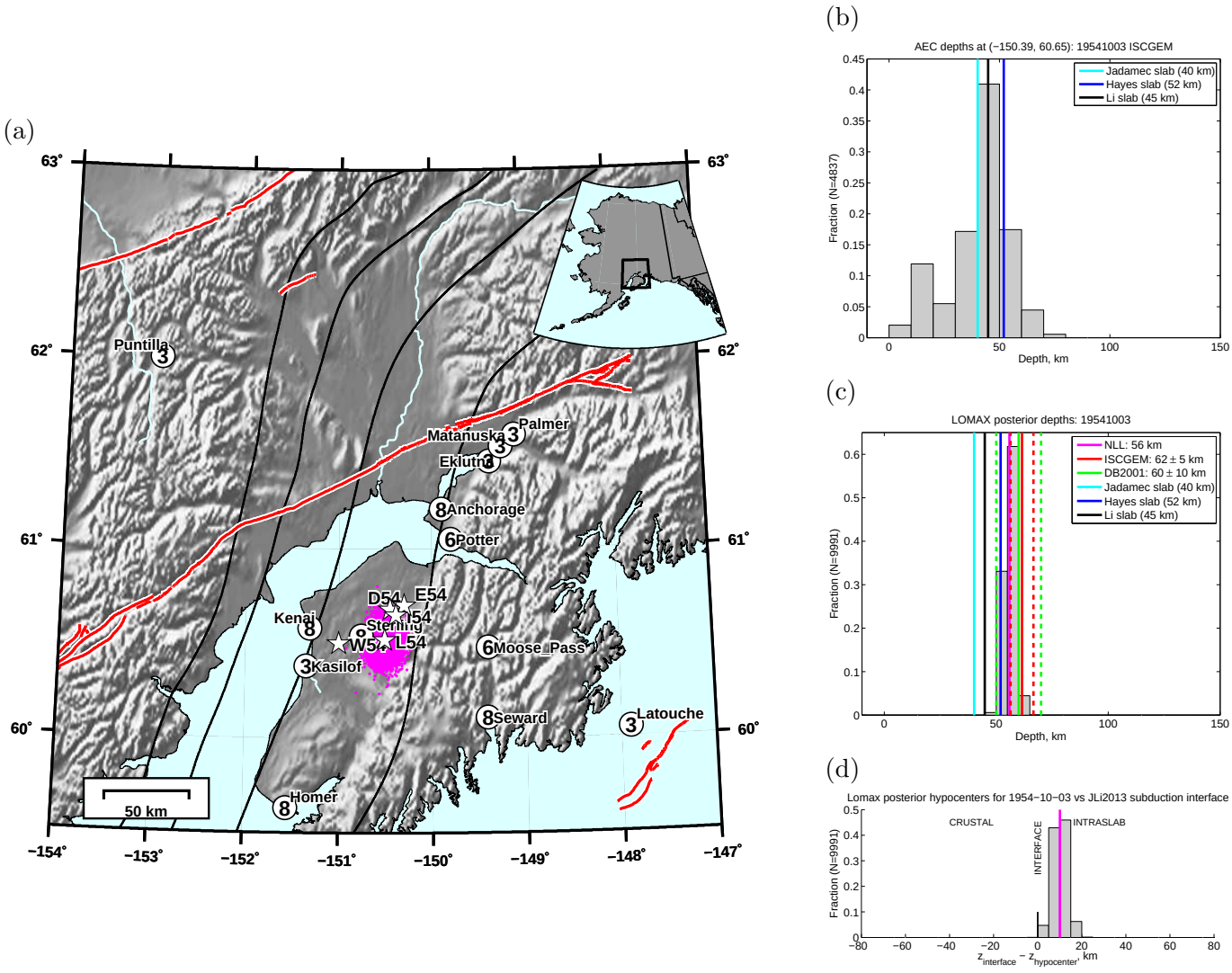

Figure B12: Event page for 19541003. See station coverage in Figure A12. (a) Posterior epicenters from NonLinLoc (*Lomax et al.*, 2000, 2014), with the star representing the maximum likelihood epicenter. Also shown are felt reports from *Brockman et al.* (1988). (b) Distribution of depths for modern seismicity (2000-01-01 to 2018-01-01, $M \geq 0$) within 40 km of the ISC-GEM epicenter. Also shown, for three subduction interface geometries, is the subduction interface depth at the ISC-GEM epicenter. The number of earthquakes in the distribution is labeled on the y-axis. (c) Distribution of depths for posterior hypocenters. Also shown are the depth estimates from NonLinLoc, ISC-GEM, and *Doser and Brown* (2001). The number of posterior hypocenters is labeles on the y-axis. (d) Distribution of the depth differences between the subduction interface, evaluated at the posterior epicenters, and the posterior hypocenters in (c).

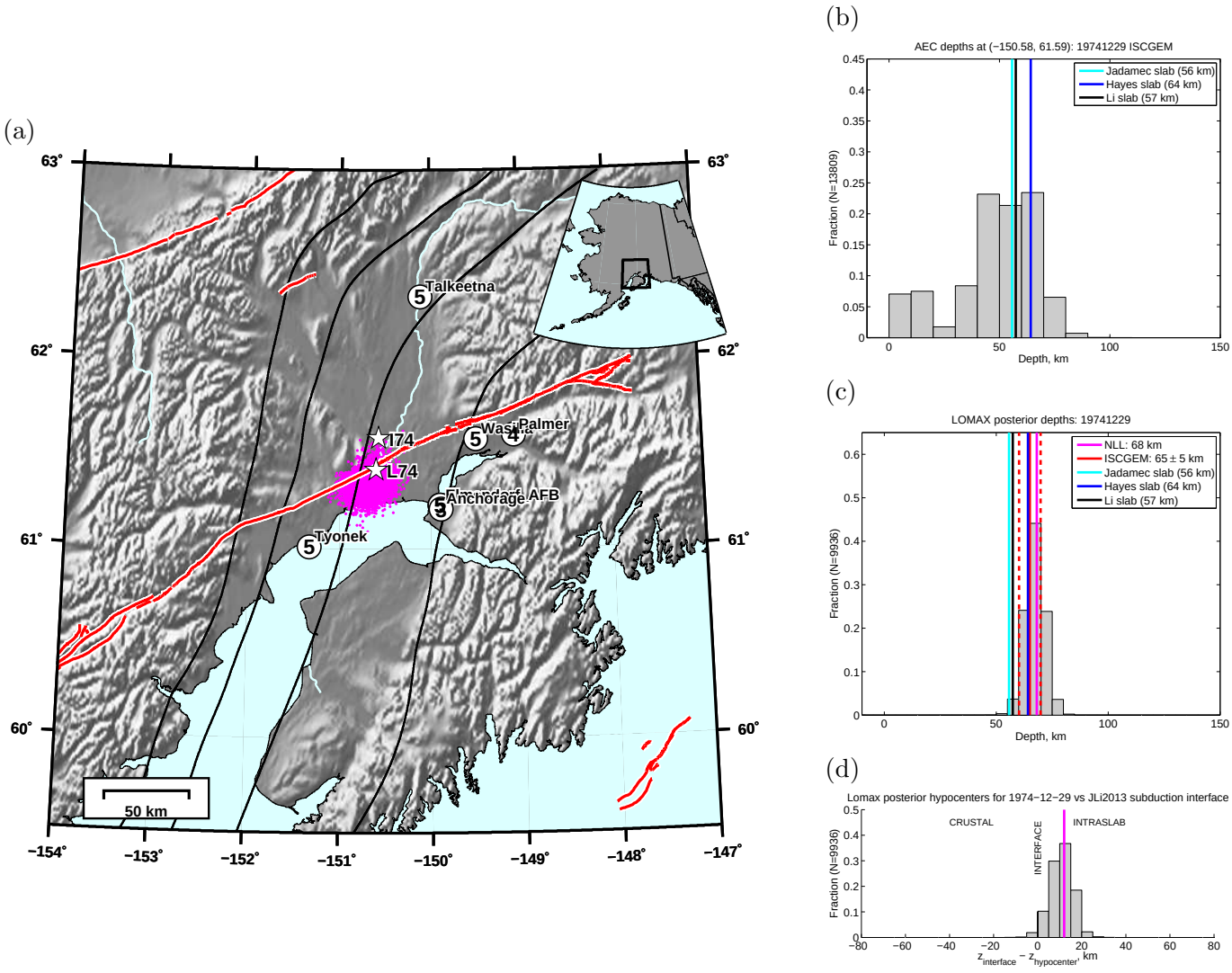

Figure B13: Event page for 19741229. See station coverage in Figure A13. (a) Posterior epicenters from NonLinLoc (*Lomax et al.*, 2000, 2014), with the star representing the maximum likelihood epicenter. Also shown are felt reports from *Brockman et al.* (1988). (b) Distribution of depths for modern seismicity (2000-01-01 to 2018-01-01, $M \geq 0$) within 40 km of the ISC-GEM epicenter. Also shown, for three subduction interface geometries, is the subduction interface depth at the ISC-GEM epicenter. The number of earthquakes in the distribution is labeled on the y-axis. (c) Distribution of depths for posterior hypocenters. Also shown are the depth estimates from NonLinLoc, ISC-GEM, and *Doser and Brown* (2001). The number of posterior hypocenters is labeles on the y-axis. (d) Distribution of the depth differences between the subduction interface, evaluated at the posterior epicenters, and the posterior hypocenters in (c).

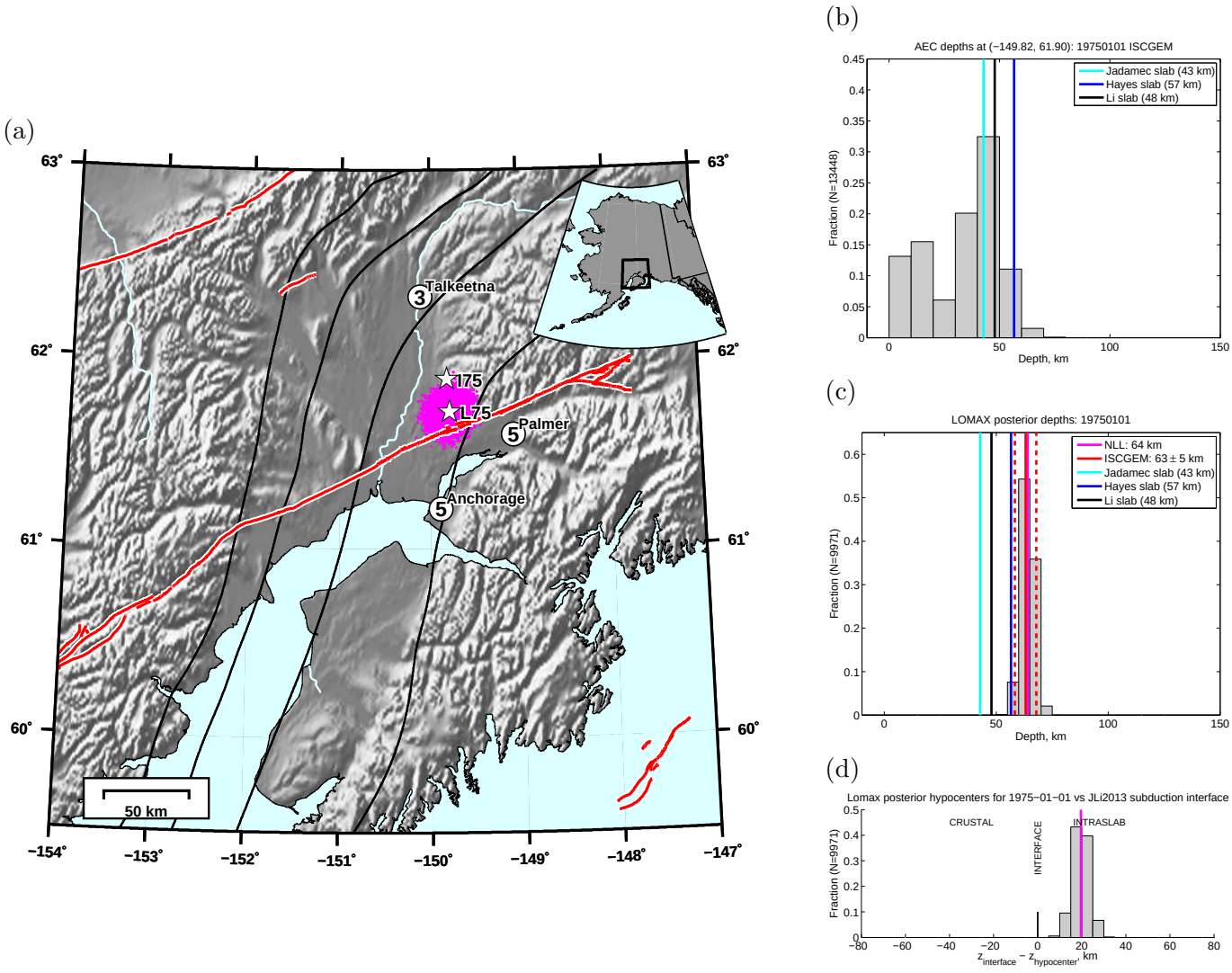

Figure B14: Event page for 19750101. See station coverage in Figure A14. (a) Posterior epicenters from NonLinLoc (*Lomax et al.*, 2000, 2014), with the star representing the maximum likelihood epicenter. Also shown are felt reports from *Brockman et al.* (1988). (b) Distribution of depths for modern seismicity (2000-01-01 to 2018-01-01, $M \geq 0$) within 40 km of the ISC-GEM epicenter. Also shown, for three subduction interface geometries, is the subduction interface depth at the ISC-GEM epicenter. The number of earthquakes in the distribution is labeled on the y-axis. (c) Distribution of depths for posterior hypocenters. Also shown are the depth estimates from NonLinLoc, ISC-GEM, and *Doser and Brown* (2001). The number of posterior hypocenters is labeles on the y-axis. (d) Distribution of the depth differences between the subduction interface, evaluated at the posterior epicenters, and the posterior hypocenters in (c).